OPTICAL AND ELECTRONIC PROPERTIES OF BULK AND MONOLAYER GERMANANE (GeH)

Dimitrios G. Lambrinoudakis

Supervisors: Prof. George Kioseoglou

Dr. Emmanuel Stratakis

Department of Materials Science Technology

University of Crete

Postgraduate dissertation

October 2018

Contents

Abstract

In recent years, there has been a resurgence of interest in studying group IV graphane analogues, a class of materials that display distinctive properties in their two dimensional form. Their exceptional electronic, optical, mechanical, chemical, and thermal properties make them highly attractive for both fundamental studies of novel phenomena and applications ranging from optoelectronic to sensing devices.

This dissertation focused on the optical properties of bulk material GeH, one material that is at the forefront of sp^3 – hybridized group IV elements. The group IV graphane analogues represent a new family of single atom-thick two-dimensional materials, in which the structure, stability and properties can be tailored for covalent ligand termination. These materials have attracted considerable interest as electronic, optoelectronic and topological devices. Firstly, bulk material samples were isolated through drop casting method and were identified via Raman Spectroscopy and Atomic Force Microscopy. The former has been widely adopted as the standard method for bulk and few-layer identification while the latter can be used to accurately determine both the vertical and lateral dimensions of nanolayered materials. The next step involved studying the optical properties of bulk crystal with respect to temperature. Therefore, samples were cooled to the liquid nitrogen temperature and their emission spectra were studied in the temperature range 80-300K using micro-Photoluminescence and μ - Reflectance Spectroscopy.

ACKNOWLEDGEMENTS

I would like to take this opportunity and mention several people who have made this dissertation possible. First and foremost, I am very grateful to my supervisor, Professor Kioseoglou, since his guidance, insight and encouragement helped me develop several skills and obtain valuable knowledge not only during this dissertation but also during my undergraduate and postgraduate years. Special regards also go to Dr. Emmanuel Stratakis for giving me the opportunity to work at the Ultrafast Laser Micro and Nano Processing Laboratory. Without them I would not have been able to be a part of the interesting and exciting field of 2D materials.

I owe my sincere gratitude to Ioanna Demeridou for always being to help me carry out the photoluminescence and reflectivity experiments. Without her effort and support I would not have been able to complete this work. I wish to thank Dr. Ioannis Paradeisanos for constructing the photoluminescence setup used during my dissertation and be willing to clarify all relevant details related to its operation. His passion for 2D materials and hit commitment to research motivated me from the beginning. I would also like to thank Myron Krassas for his assistance during the AFM measurements nd Kostas Orfanakis for our conversations at the early stages of my dissertation that really helped me understand the importance of asking questions and seeking out the answers. Beside the technical aspect, the time I spent together with these individuals in the lab and our discussions certainly made this journey more enjoyable.

Finally, I am indebted to my family for their constant support. I owe so much to my parents, George and Kalliopi, for supporting me to all the way and believing in me when I did not. I am grateful for my brother, Theo, who has always been an example to me. Without their help, motivation and continued encouragement I wound not have been a person that I am today.

A final thanks goes to my friends, especially Tasos, Stamatis, Maria, Stauroula, Vaggelio, for always being there to support me.

List of Figures

Part I:
Introduction

sp^3 – hybridized group IV elements 1

1.1 Overview

Silicon and germanium, the workhorse materials of the semiconductor industry, are the most important and ubiquitous materials of the current era. Still, the never-ending push toward device miniaturization calls for decreasing the size of electronic channels. The past decade has witnessed the creation of two-dimensional (2D), or single-atom-thick materials, which have led to the discovery of new phenomena and properties that are not present in the parent three-dimensional (3D) materials[1-4] Furthermore, the creation of single-atom thick derivatives of silicon and germanium oriented in a honeycomb arrangement are predicted to have direct band gaps compared to the indirect gap in the bulk of silicon and germanium, opening up light-emission based applications for these materials[5]. Consequently, the creation of stable, robust single-atom thick 2D sheets of these semiconductor materials would have enormous implications in the electronics and optoelectronic industries.

The focus of this dissertation involves the optical properties of functionalized germanium Graphane analogues such as Germanane (GeH). In this chapter, we summarize the development of 2D materials, such as group IV graphane analogues and describe the crystal and electronic structure, the vibrational and the optical properties of hydrogenated germanium. .

1.2 Crystal structure

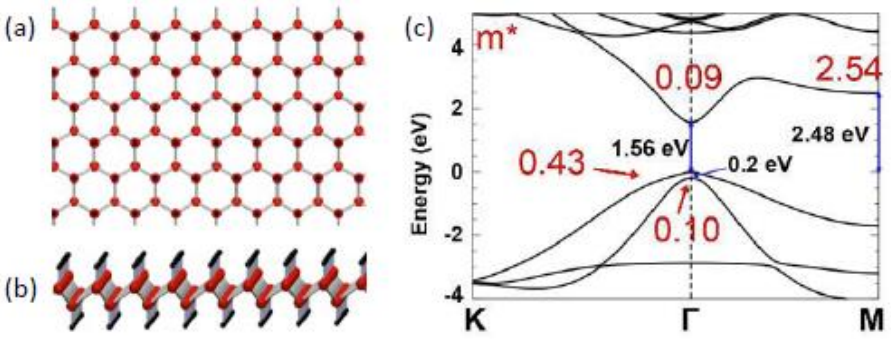

Figure 1.1: (a) Top view of GeH (b) side view of GeH (c) band structure of GeH adapted from [6]

Germanane is the germanium analog of graphane, hydrogen terminated graphene. It is a buckled honeycomb of germanium that is stabilized by one hydrogen per germanium atom as seen in Figure 1.1a and 1.1b. It has a direct bandgap at the Γ-point (Figure 1.1c) that can be tuned via surface covalent functionalization [6, 9, 12]. Additionally, germanane is stable in air and has a high predicted mobility of 18,000 cm^2 /V*s at room temperature, making it extremely promising for electronic and optoelectronic applications [6, 12] Specifically, the combination of high mobility, non-zero bandgap, and low dimensionality are advantageous for short channel field effect transistors (FETs) with high on-off ratios and low quiescent currents [11]. Furthermore, germanane's large spin orbit coupling makes it possible to explore novel physical phenomena such as quantum spin Hall effect at room temperature [7,10,13].

One of the biggest challenges realizing germanane's exciting properties is the creation of single layer material. Bianco *et al* [6] successfully isolated single layer germanane from bulk crystals using micro-mechanical exfoliation. These flakes were small and difficult to produce. A much more robust way to synthesize germanane is needed. Chapter 1.3 describes a method to produce large area thin germanane by molecular beam epitaxy (MBE) that is hoped to soon be extended to single layer germanane.

1.3 Synthesis of GeH

The synthesis of stable multilayers of hydrogenated germanene requires a relatively sophisticated process when compared to the synthesis of other Group IV 2D materials such as graphene and silicene. Although $CaGe_2$ has been known since 1944[17] monolayers of germanium have only recently been developed. A standard method to synthesize germanane through the deintercalation of $CaGe_2$ was recently proposed by Bianco et al. [6].

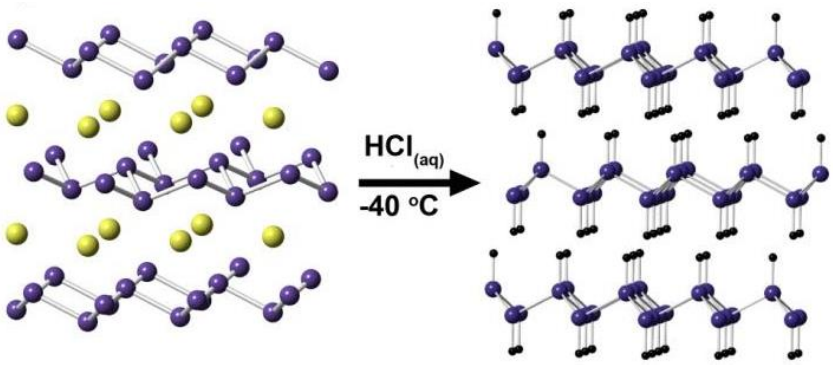

Figure 1.2 Scheme of topotactic deintercalation of $CaGe_2$ into GeH.

The synthesis of germanane took place in a two-step process. The first step was to synthesize a $CaGe_2$ zintl framework in which the Ge atoms are arranged in a plane. This planar arrangement ultimately assists in forming the 2D Ge sheet. For this step, Ca and Ge were loaded in stoichiometric amounts into a quartz tube. As the synthesis of $CaGe_2$ is highly oxygen-sensitive [8] strict air-free procedures were used and a Schlenk line was used to evacuate the quartz tube which was then sealed using a MAP/Pro oxygen torch. The mixture was annealed at 1050 _C for 18–20 h, and cooled over 7 days forming $CaGe_2$ crystals.

The second step was to deintercalate the Ca ions from the $CaGe_2$ system by placing the crystals in a solution of concentrated HCl (35%) and stirring continuously for 8 days at _40 _C. Using this method, the possible mechanism of intercalation for the synthesis of Ge-H can be summarized as follows:

$$\mathbf{n(CaGe_2) + 2n\ HCl \ \downarrow (GeH)n + nCaCl_2:}$$

Following the 8-N rule of Zintl phases [15] the strong heteropolar bonding character in $CaGe_2$ leads to the formation of puckered (Ge-)n polyanion layers, which are separated from each other by planar monolayers of Ca^{2+} ions.

We should point out that this reaction mixture was washed with Milli-Q H_2O and methanol and then dried at room temperature. Both the excess acid and the $CaCl_2$ byproducts of the reaction were removed by the wash, as calcium chloride is a typical ionic halide and is highly soluble in water.

1.4 Electronic Band Structure

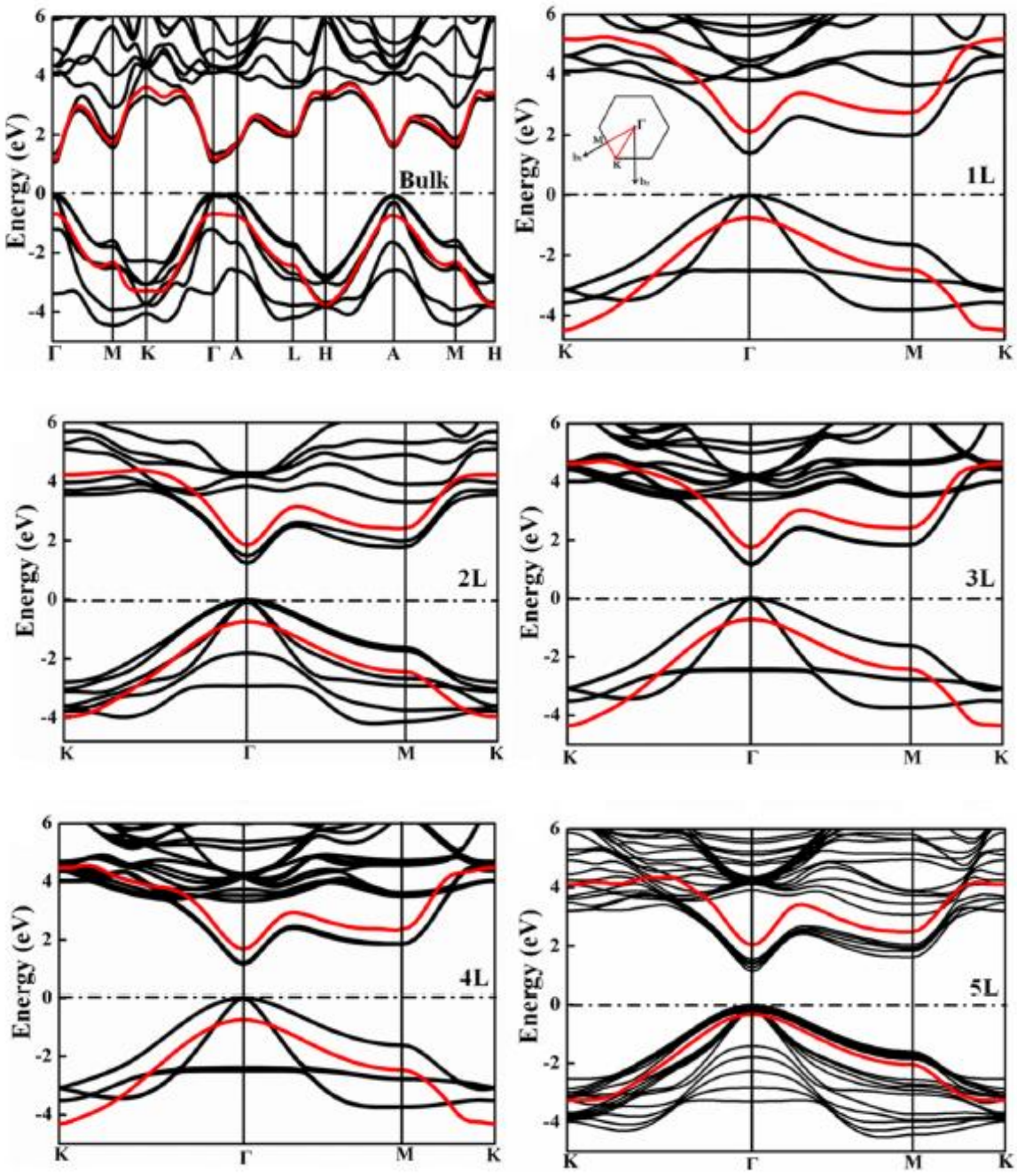

Figure 1.3 Band structures of bulk and 1L−5L germanane from LDA (black solid lines) and G_0W_0 (red solid lines) calculations. Only the uppermost valence band and lowest conduction band of G_0W_0 results are plotted for clarity [19]

The electronic band structure of bulk germanane is presented in Figure 1.3, which exhibits semiconducting nature. A direct band gap appears at the Γ point, and the self-energy correction enlarges the band gap from the DFT value of 1.06 to 1.86 eV, well

reproducing the measured value of 1.70 eV [19]. The topology of the band structures of 1L−5L germanane is very similar except that the direct band gap at the Γ point decreases with increasing the stacking layer. This may stem from the fact that the conduction band minimum (CBM) and valence band maximum (VBM) of few-layer germanane have different thickness-dependent behavior.

CBM shows a relatively quick upshift, while VBM shifts down smoothly as the stacking layer decreases (Figure 1.4a), which eventually results in the increasing band gap in few-layer germanane. This is further reflected from the partial charge density, in which the change in CBM is prominent while that in VBM is insensitive to the thickness (Figure 1.4b). More interestingly, the thickness dependence of the band gaps in few-layer germanane can be fitted according to a power law with the formula $E_g(N) = A + B/N^{\beta}$, where $E_g(N)$ and A are the band gap of the NL germanane and bulk germanane, respectively, and N is the layer number,B is constant for the fitting results.

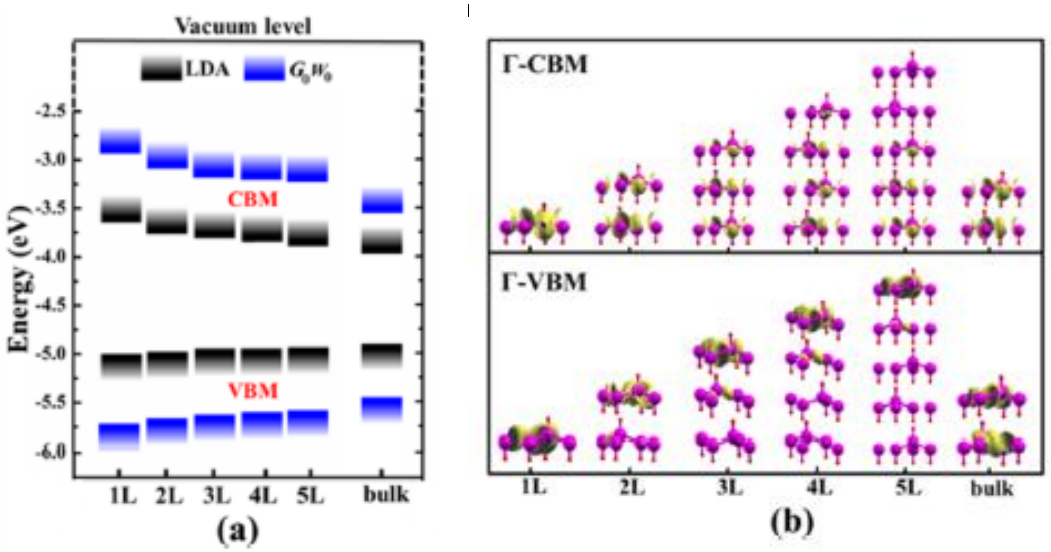

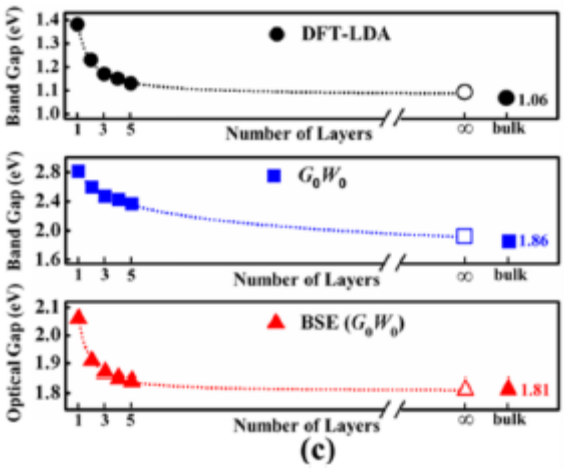

Figure 1.4. (a) VBM and CBM with respect to the vacuum level in few-layer and bulk germanane and (b) the partial charge density of VBM and CBM. (c) The LDA, G_0W_0 band gaps, and optical gap (i.e., first optical absorption peak) of few-layer and bulk germanane (solid). The power law fitting curves are presented by dashed lines. Hollow circles, squares, and triangles correspond to the fitting values of bulk germanane from the scaling laws.

1.5 Optical properties

The optical properties of germanane were investigated by DRA method (Deformation Rate Analysis) [9]. This silver-black material has a broad absorption over visible wavelengths, and a linear approximation of the absorption edge suggests a band gap of approximately 1.59 eV (Figure 1.4). The Tauc/Davis-Mott expression for materials with 2D densities of states predicts that the absorbance A($\hbar\omega$) at photon energy $\hbar\omega$ near the band edge would be a step function with a discontinuity in absorbance at the band gap if the band gap was direct allowed. If the band gap was indirect, the absorbance would be proportional to $\hbar\omega$ – Eg' ± Ep, where Eg' is the indirect gap and Ep is the energy of a particular phonon mode. However, it has been experimentally established that the Tauc/Davis-Mott approximations of absorption cannot unambiguously determine the transition mechanism for fundamental absorption for bulk materials with 2D densities of states [17-19]. The absorbance was modeled assuming direct-allowed, direct-forbidden, indirect-allowed, and indirect-forbidden gaps using both 2D and 3D densities of states (Figure 1.5). All of these plots estimated fundamental gaps ranging from 1.48 to 1.60 eV. These analyses are complicated by a broad Urbach edge at the lower end of the absorption tail, which is

often indicative of a large doping concentration or disorder. The presence of photoluminescence is often a stronger test of a direct band gap. Previously reported studies of GeH thin films proposed that GeH is a direct band gap material with a fundamental absorption gap at 1.8 eV based on photothermal deflection spectroscopy and photoluminescence that occurs at 0.45 eV lower, or 1.35 eV[20] About their measurements of the experiments they did not observe any photoluminescence from 1.1 to 1.8 eV when exciting from 1.38 to 1.96 eV at temperatures ranging from 14 to 300 K. This lack of photoluminescence and linear slope in their samples might suggest that germanane has an indirect band gap. However, the lack of photoluminescence alone is not sufficient evidence of an indirect gap. A direct band gap material could lack photoluminescence if there is a large concentration of nonradiative defect states or impurities in the sample or if the material possesses unique surface or edge states. The presence of any of these can quench photoluminescence and also contribute to the observed bowed Urbach edge. Therefore, further optimization of the growth and etching chemistry will be necessary before dismissing the potential existence of a direct band gap. Also, they propose that more direct measurements, such as angle-resolved photoemission spectroscopy, as well as additional temperature-dependent absorption studies are necessary to completely conclude whether germanane has a direct or indirect band gap, especially since theory predicts GeH to have a direct band gap.

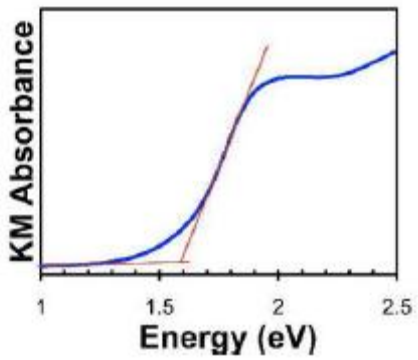

Figure 1.5 DRA of GeH. *(a) DRA spectrum of GeH plotted as hνα vs photon energy highlighting a 1.59 eV band gap.*

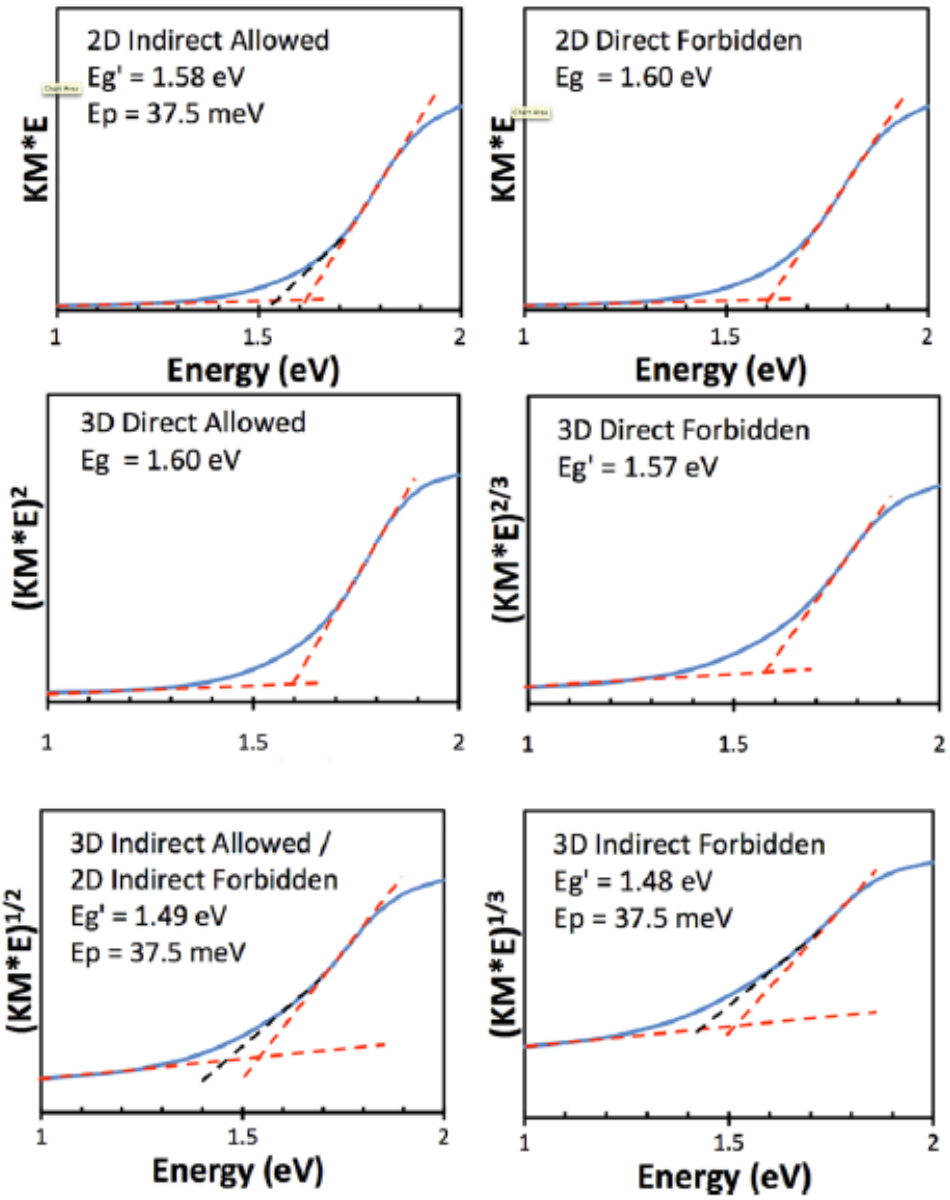

Figure 1. 6 Absorption spectrum of GeH fitted to different band structures. *The fitting is according to Tauc/Davis-Mott expressions of 2D densities of states and 3D densities of states and a 37.5 phonon vibration (deduced via the 300 cm-1 Raman shift) was determined.*

Band structure calculations suggest that germanane is a direct band gap material both as isolated layers and in the crystal structure having two layers per unit cell. Density functional theory (DFT) code VASP was used [15, 16] to optimize the geometry and calculate the band structure of isolated single layer and two-layer unit cell GeH. The interactions between cores and electrons were described for relaxation by projector augmented wave (PAW) pseudopotentials [21] within the PBE exchange-correlation function [22, 23] with a plane-wave cutoff energy of 600 eV. van der

Waals interactions between the layers were included using the DFT-D2 method by Grimme[24] For the two-layer structure, the unit cell was modeled as a P63mc unit cell with relaxed lattice parameters of a = 4.05 Å and c = 10.56 Å, thus having a 5.3 Å layer spacing. For the isolated single-layer structure, the calculations were performed in a unit cell with 20 Å of additional vacuum between GeH layers. To obtain an accurate description of the band gap in this system, the hybrid HSE06 [25-27] exchange-correlation function was used. With this function, it has been obtained a direct gap at the Γ point of 1.56 eV for an isolated layer (Figure 1.1c) and 1.53 eV for the bilayer , which is in excellent agreement with the observed experimental band gap. The calculated band gap for the two-layer unit cell at the A point of the Brillouin zone is ~1.77 eV. The difference in energy between the conduction band minimum at the M point and the valence band maximum at Γ is 2.48 and 2.33 eV for an isolated layer and two-layer unit cell, respectively. In both cases, spin-orbit splitting at the Γ valence band maximum is 0.2 eV.

1.6 Air stability of GeH

The potential utility of germanane for any optoelectronic or sensing device strongly hinges on its air and temperature stability. Some previous reports state that hydrogen-terminated Ge (111) surfaces having the same atomic configuration as GeH are resistant to oxidation when the Ge surface has minimal defects, although some debate remains [14, 28, 29]. Because FTIR spectroscopy is a sensitive probe of the presence of Ge-O vibrational modes at 800-1000 cm^{-1}, GeH samples were exposed in air for a series of times and the FTIR was measured under the attenuated total reflectance (ATR) mode. Virtually no change from 800 cm^{-1} to 1000 cm^{-1} was observed after 60 days' air exposure, thus proving that the bulk of GeH resists oxidation (Figure 1.6a). Additionally, time-dependent XPS was performed to probe changes in the Ge oxidation state of the surface after exposing these layered GeH crystals to air (Figure 1.6b), and the percentage of each germanium oxidation state for all spectra was calculated by applying a standard Gaussian fit. After 1 month of exposure to air, a $Ge^{2+/3+}$ shoulder emerges at ~1219.3 eV (19.5% $Ge^{2+/3+}$). This peak becomes more intense after 5 months of air exposure (29.7% $Ge^{2+/3+}$). After Ar

etching the top 0.5 nm (<1 layer), the $Ge^{2+/3+}$ almost completely disappears with 10.1% $Ge^{2+/3+}$ remaining. Together, the XPS and FTIR suggest that only the surface of GeH becomes oxidized over time, while the bulk is resilient to oxidization.

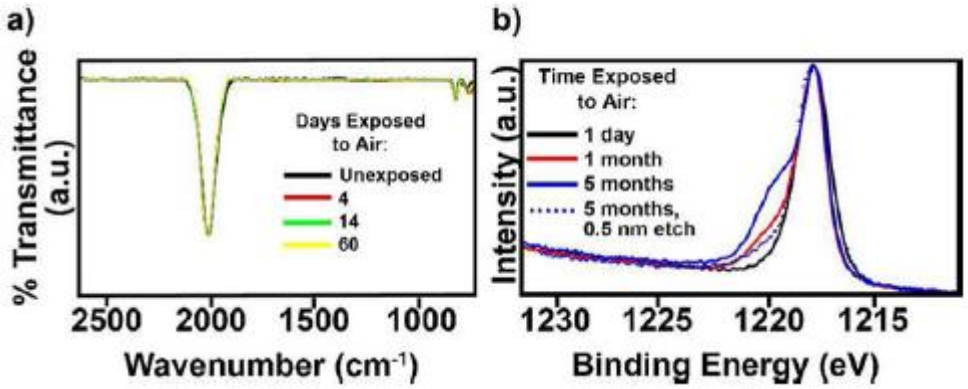

Figure 1.7 Air stability of GeH. *(a) Time-dependent FTIR of a GeH flake after exposure to ambient atmosphere for up to 60 days, collected via reflection mode, highlighting minimal changes in the relative intensity of the Ge-H to Ge-O vibrations. (b) Time-dependent Ge 2p XPS spectra of germanane immediately after exposure to atmosphere, after 1 day, 1 month, 5 month and after 5 months, followed by Ar etching by 0.5 nm.*

Theory of Raman and Photoluminescence Spectroscopy 2

2.1 Raman Spectroscopy

Vibrational spectroscopic methods constitute a powerful tool in analyzing some of the most fundamental processes in physical chemistry: molecular vibrations. These methods measure vibrational energy levels which are associated with chemical bonds and provide information about the molecular composition, structure and interactions within the sample. Vibrational spectroscopy can be used for a wide range of applications in material characterization such as sample identification and quantification, crystal structure and quality determination, reaction monitoring etc. While there are various experimental techniques used to analyze those vibrations, most are variations of Raman and Infrared (IR) spectroscopy.

When light interacts with matter, the photons which make up the light may be reflected, absorbed, transmitted or scattered. Scattering is the phenomenon in which light changes direction and possibly also its frequency after interacting with the studied medium. The scattered radiation is considered to be elastic if its frequency remains unchanged or inelastic if the frequency changes in the process. The basic principle behind Raman spectroscopy is the detection and analysis of inelastically scattered light from the medium, produced by the interaction of light with the atomic or molecular vibrations. Inelastic scattering was first observed in molecules by C.V. Raman and K.S. Krishnan in 1930 [31] and since then it has been proven as a useful tool in probing the fundamental excitations in matter.

According to classical theory [32], Raman scattering can be explained as follows: The electric field strength (E) of the electromagnetic wave (usually a laser beam) oscillates with time (t) as shown by Eq. (2.1):

$$E = E_o \cdot \cos(2\pi \cdot f_o \cdot t) \quad (2.1)$$

where E_o is the vibrational amplitude and f_o is the laser frequency. When a molecule is irradiated by this light, a subsequent electric dipole moment p is induced which is directly proportional to the electric field:

$$p = \alpha \cdot E \quad (2.2)$$

The proportionality constant α is called polarizability of the molecule and describes how easily the molecule can be deformed i.e. the tendency of its charged distribution to be displaced by the external electric field. It highly depends on the shape and dimensions of the chemical bonds and in the general case, is a tensor because molecules tend to polarize more readily in some directions thanothers. Given the fact that chemical bonds change during vibrations, the polarizability is dependent

on molecular vibrations. In other words, it depends on the normal coordinate Q of the molecule:

$$Q = Q_o \cdot \cos(2\pi \cdot f_{vib} \cdot t + \varphi) \quad (2.3)$$

Here, Q_o and f_{vib} are the vibrational amplitude and frequency, respectively, and φ is a phase angle.For a small amplitude of vibration, α is a linear function of Q. Thus, we can write:

$$\alpha = \alpha_o + \sum_k \left(\frac{\partial \alpha}{\partial Q_k}\right)_o \cdot Q_k + \frac{1}{2} \cdot \sum_{k,l} \left(\frac{\partial^2 a}{\partial Q_k \partial Q_k}\right)_o \cdot Q_k \cdot Q_l + \ldots \quad (2.4)$$

where, α_o is the polarizability at the equilibrium position and Q_k and Q_l are the normal coordinates that correspond with the k^{th} and l^{th} normal vibrations with frequencies f_k and f_l. In a first approximation, only the first two terms will play a significant role. Therefore, considering the v^{th} normal vibration, Equation (2.4) is modified to:

$$\alpha = \alpha_o + \sum_k \left(\frac{\partial \alpha}{\partial Q_k}\right)_o \cdot Q_k = \alpha_o + \alpha_v' \cdot Q_v \quad (2.5)$$

Substitution of Equation (2.3) to (2.5) yields:

$$\alpha_v = \alpha_o + \alpha_v' \cdot Q_o \cdot \cos(2\pi \cdot f_v \cdot t + \varphi) \quad (2.6)$$

By combining (2.1) and (2.6) with (2.2), we obtain:

$$p = \alpha_o \,.\, Eo \cdot \cos(2\pi \cdot fo \cdot t) + \alpha_v' \cdot Q_o \cdot E_o \cdot \cos(2\pi \cdot f_v \cdot t + \varphi) \cdot \cos(2\pi \cdot f_o \cdot t) \quad (2.7)$$

By using the trigonometrical formula:

$$cosA \cdot cosB = \frac{1}{2}(\cos(A+B) + \cos(A-B)) \quad (2.8)$$

the previous equation can be written as:

$$p = \alpha_o \cdot E_o \cdot \cos(2\pi \cdot f_o \cdot t)$$

$$+ (1/2) \cdot \alpha_v' \cdot Q_o \cdot E_o \cdot \cos[2\pi \cdot (f_o - f_v) \cdot t - \varphi]$$

$$+ (1/2) \cdot \alpha_v' \cdot Q_o \cdot E_o \cdot \cos[2\pi \cdot (f_o + f_v) \cdot t + \varphi] \quad (2.9)$$

According to classical theory, the induced dipole moment consists of three terms. For clarity, equation is rewritten as a function of frequencies f_o and f_v:

$$p = p_1(f_o) + p_2(f_o - f_v) + p_3(f_o + f_v) \quad (2.10)$$

The first term represents the case of elastic scattering, where an oscillating dipole radiates light of frequency equal to that of the external electromagnetic radiation, fo. This type of elastic scattering is called Rayleigh scattering and does not involve any

energy change between the incoming and scattered radiation. The last two terms describe the inelastic or alternatively called Raman scattering. In particular, the second term corresponds to the so-called Stokes scattering where the frequency is reduced by a factor of fv, implying that the scattered photon has lost energy to the molecule. In contrast, during an Anti-Stokes process the photon has gained energy, hence its higher frequency $f_o + f_v$. If $\alpha_v' = (\partial\alpha/\partial Q)_o$ is zero then $p = p_1(f_o)$ and all the scattered radiation originates from elastic processes. In that case, the vibration is said to be Raman-Inactive. To be Raman-active, the rate of change of polarizability with the vibration must not be zero.

Now that Raman effect has been derived using the classical theory, we can use the quantum theory to better visualize the process and determine additional information (See Fig. 2.1) [32-33]. According to the quantum interpretation, radiation is emitted or absorbed as a result of a system making a downward or upward transition between two discrete energy levels. When light is incident on our system, a short-lived state called a virtual state is formed in which the molecule is being excited. This state is not stable, and the photon is quickly re-radiated. When this occurs, there are three potential outcomes. Firstly, the molecule can relax back to its ground electronic state and emit a photon of equal energy to that of the incident photon (Rayleigh scattering). Secondly, the molecule can relax to a real vibrational state and emit a photon with less energy than the incident photon (Stokes scattering). The third possible outcome is that the molecule is already in an excited vibrational state, is excited to a higher virtual state, and then relaxes back down to the ground state emitting a photon with more energy than the incident photon (Anti-Stokes scattering). In the last

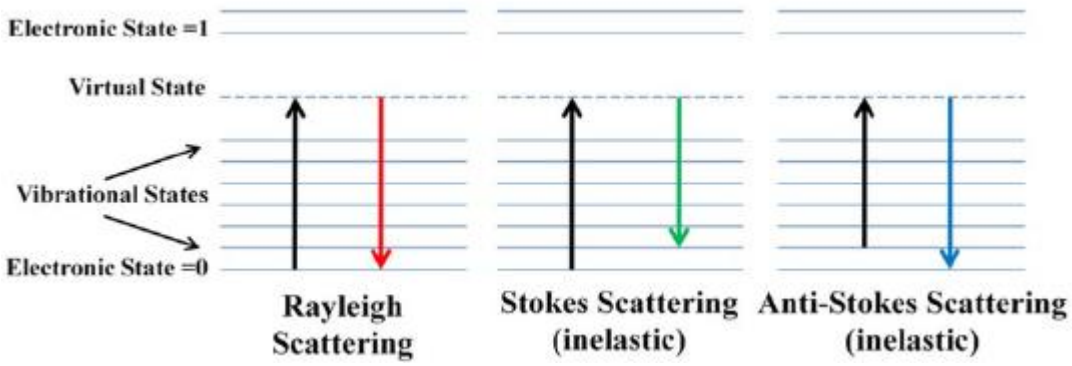

Figure 2.1: Jablonski diagram representing quantum energy transitions for Rayleigh and Raman Scattering. The dotted line indicates a virtual state to distinguish it from real excited states [77].

two cases, the scattered radiation is what we measure experimentally as Raman scattering and the energy difference between the excitation and scattering process corresponds to the energy of vibrations of the molecule. Raman scattering is inherently a weak process as only a small fraction of light (approximately 1 in 107 photons) is inelastically scattered. The intensity of Raman peaks is defined by the next equation [31]:

$$I = K \cdot a^2 \cdot P \cdot \frac{1}{\lambda^4} \quad (2.11)$$

where K is a proportionality constant, α is the polarizability, P is the laser power and λ is the wavelength of incident photons. Therefore, only the last two parameters are under the control of the spectroscopist, who can tune them to constitute Raman scattering as a non-negligible scattering mechanism.

A typical Raman spectrum illustrates the intensity of the scattered light as a function of it frequency or, more commonly, wavenumber difference to the incident radiation. Peaks corresponding to Stokes and Anti-Stokes processes appear symmetrically around the laser line but the relative intensities depend on the initial population of the various states of the molecule which in turn depends on temperature. According to Maxwell‑Boltzmann statistics, the lower state will be more populated than the upper state in thermodynamic equilibrium. Consequently, most molecules will be found in the ground state at room temperature, thus anti-Stokes scattering will be substantially weaker than the Stokes Raman scattering. Most Raman measurements are performed considering only the Stokes shifted light.

In this section so far, Raman scattering has been described in terms of the first-order contribution, in which only one vibrational unit is emitted or absorbed. In solids, normal vibration modes are quantized by quasiparticles called phonons. Under the restriction of momentum conservation, this process involves only phonons with wavevector $q \approx 0$ (i.e. the center of the Brillouin zone) due to the negligible momentum of light. In contrast, second-order Raman processes include features coming from different crystalline momenta, potentially from the entire Brillouin zone. For two different phonons with frequencies f_a and f_b and wavevectors q_a and q_b, peaks with Raman frequencies $f_a + f_b$ and $f_a - f_b$ are referred to as the combination and

difference modes, respectively. Wavevector conservation in two-phonon Raman scattering is satisfied when $q_a \pm q_b \approx 0$. If the two phonons are identical, the resultant two-phonon Raman peak is known as an overtone. In overtone scattering the aforementioned condition implies $q_a = - q_b$, i.e. the two phonons have equal and opposite wavevectors. Thus, in two-phonon Raman scattering there is no restriction on the magnitudes of the individual phonon wavevectors as there is in one-phonon scattering (only their sum must be near zero). Second-order Raman scattering is usually much weaker than first order scattering, but can be enhanced by various mechanisms [31]. When the energy of the incoming light coincides with an electronic transition, the system is excited not to a virtual but an electronic state and the absolute Raman intensities can be enhanced by several orders of magnitude. This variation is called Resonance Raman [32-33].

Infrared spectroscopy also measures the vibrational energies of molecules. The basic principle behind IR spectroscopy is the measurement of absorption of infrared light by the sample as a function of frequency. In particular, infrared energy covering a range of frequencies is directed onto the sample. Absorption occurs where the frequency of the incident radiation matches that of a vibration so that the molecule is promoted to a vibrational excited state. The loss of this frequency of radiation from the beam after it passes through the sample is then detected.

The main difference between the two spectroscopic methods is manifested in the different selection rules applying to each one. As previously mentioned, for a vibration to be Raman active there must be a change in the polarizability of the molecule during this vibration. On the other hand, an IR transition is detected when the molecule undergoes a dipole moment change during the vibration. For instance, when studying symmetrical molecules, e.g. O_2, we cannot observe any IR lines as the molecule is unable to change its dipole moment. Another difference can be found in the excitation source. Modern Raman spectroscopy uses a monochromatic laser beam in the visible, near-infrared, or near ultraviolet region of the electromagnetic spectrum. This is not the case for IR spectroscopy where a laser beam is used in the infrared regime. The wavelength is changed over time, thus allowing the observation of all the absorption lines within the studied range of the infrared region. Unlike infrared absorption, Raman scattering does not require matching of the incident

radiation to the energy difference between the ground and excited electronic states [32-33].

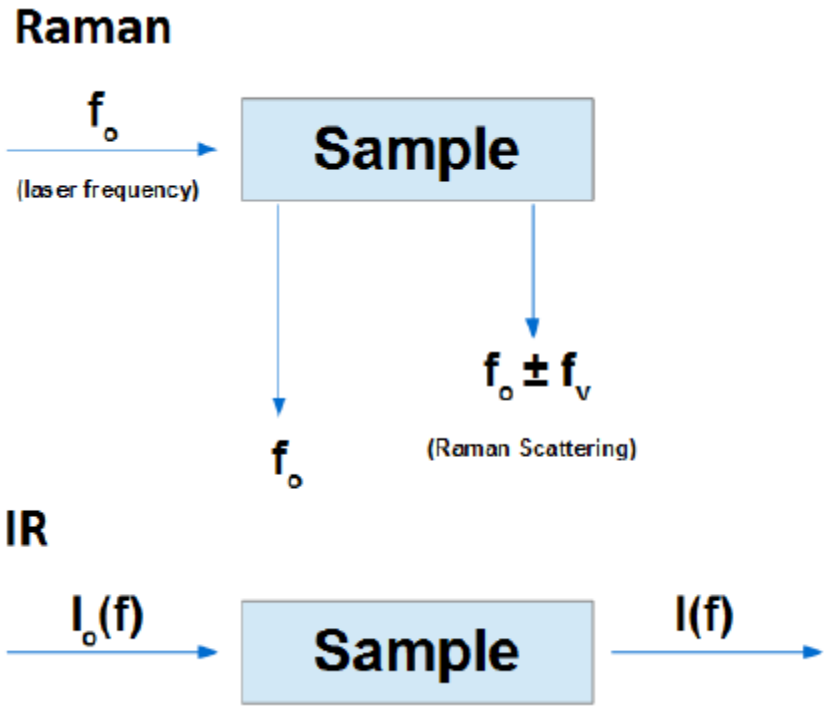

Figure 2.2: Illustration of Raman and IR vibrational spectroscopies. In the bottom figure, I_o and I denote the intensities of the incident and transmitted beams, respectively.

2.1.1 Electronic band structure and phonon dispersion of GeH in comparison of silicane.

The calculated electronic band structure for silicane and germanane are plotted in figure 2.3. In comparison to graphene [38] one important difference in silicane and germanane is that in the latter two materials a band appears close to the conduction band edge at the M point. While the conduction band minimum of Ge_2H_2 is at the Γ point similar to C_2H_2, in the case of Si_2H_2 it is in fact at the M point, making silicane an indirect gap semiconductor. The band gaps of silicane and germanane are 2.91 eV and 1.90 eV, respectively, according to the HSE06 functional which is expected to

underestimate the gap by no more than 10% [39]. Note that the conduction band is anisotropic at the M point with a heavy effective mass in the Γ direction. The fact that the band gap of Si_2H_2 is indirect and that of Ge_2H_2 is direct is supported by previous works using a variety ofmethods ranging from semi-local DFT through hybrid functionals to single-shot GW
[34, 36, 37].

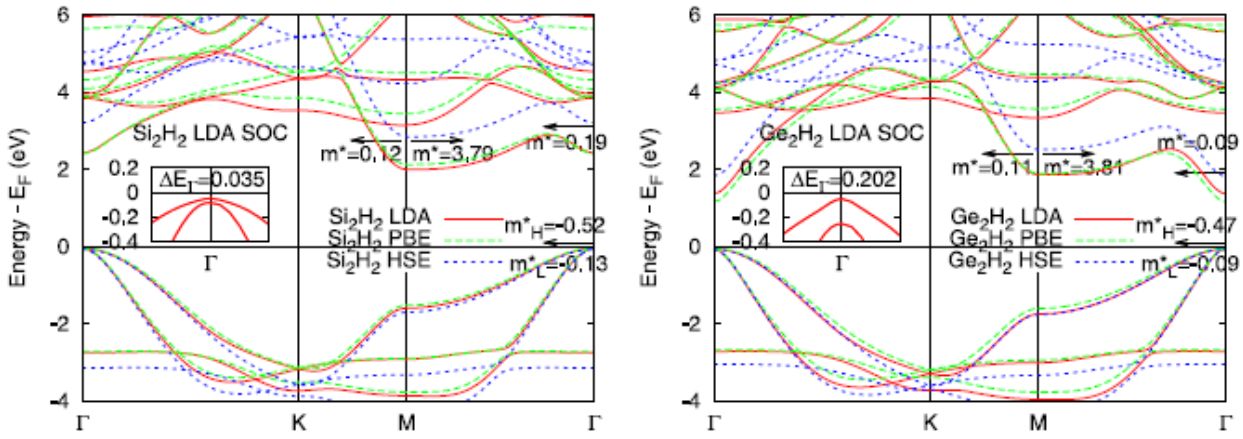

Figure 2.3. Band structures of silicane and germanane. The zero of energy is taken to be the Fermi level and the top of the valence band is marked with a horizontal line. The effect of spin–orbit coupling at the Γ point is illustrated in the insets. Effective masses (in units of electron mass) in the HSE06 calculations are provided in the conduction band at M and Γ, and in the valence band at Γ (where the H and L subscript refers to the heavy and light effective mass).

The HSE06 band structures were used as reference to obtain the tight-binding parameters. It was found that the tight-binding band structure can reproduce the entirety of the DFT valence band and the vicinity of the conduction band at both the Γ and M points (see figure 2.4). It is important to note that if second-nearest neighbor interactions were neglected, the valence band can still be reproduced but, on the other hand,the behavior of the conduction band at the M point cannot indicating that the second nearest neighbor interactions are responsible for the minimum in the conduction band at the M point. Also, the d-shell of Si/Ge is likely to affect states in the conduction band.

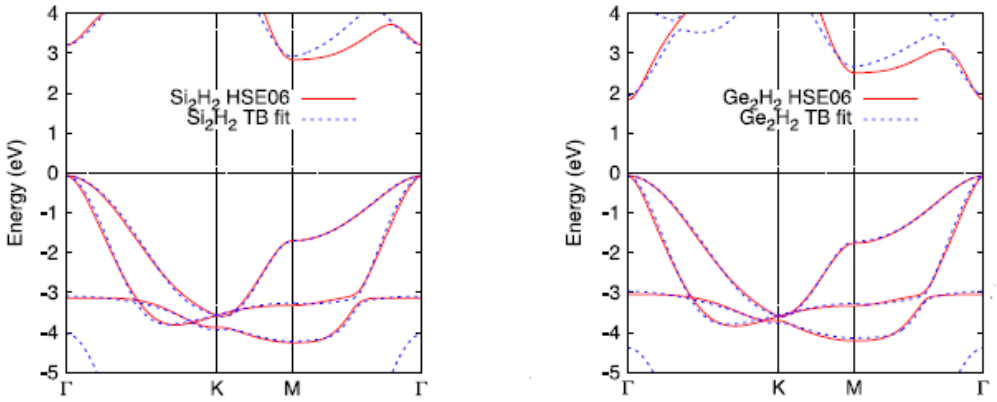

Figure 2.4. Tight-binding band structures of silicane and germanane compared with theHSE06 DFT bands.

Finally, it has been performed a full geometry optimization of Si_2H_2 and Ge_2H_2. While the geometry optimization yields an energetically stable configuration for both materials, it is necessary to examine their phonon dispersions in order to ascertain whether they are dynamically stable. Silicane is stable as there is no sign of any dynamical instability anywhere along the high symmetry lines of the Brillouin zone (see figure 2.4). In the case of Ge_2H_2, a small pocket of instability for the flexural acoustic phonons was found but it was believed that this was an artifact arising due to the difficulty in converging the flexural acoustic branch of 2D materials as the phonon wave vector goes to zero. Since finding no other pockets of instability in any of the other branches it was concluded that germanane is also dynamically stable. This is unimportant finding as the experiments in [18] were performed on multilayers of germanane on a substrate, while calculations predict that suspended single-layer germanane would be stable, too.

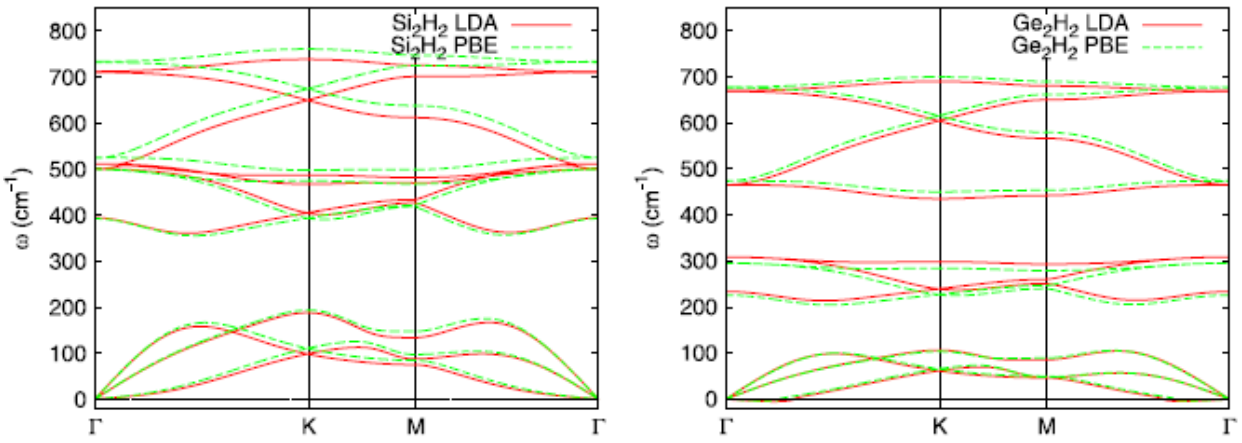

Figure 2.5. Phonon dispersions of silicane and germanane.

In figure 2.5 we see the phonon dispersion of silicane and germanane. Two main vibrational modes have appeared. As we see in 228cm^{-1} and 302 cm^{-1} which are in agreement with the experimental results we will describe in this thesis later in session 4.2 in Raman spectra.

2.1.2 Raman spectroscopy of GeH

The Raman spectroscopy of isolated GeH flakes show subtle differences between the 1T and 6R GeH phase and a much larger change in the 2H phase. As expected, the incorporation of the heavier Ge atom onto the germanane framework causes the Raman modes to shift to lower wavenumbers. In the Raman spectra (Figure 2.6), the intense in-plane Ge−Ge E_2 modes for 1T and 6R GeH occur at 301.6 and 301.8 cm^{-1}, respectively, while the 2H phase shifts to 300.2 cm^{-1}. Furthermore, the out of- plane A_1 mode for the 1T and 6R GeH phases both occur at 227.7 cm^{-1}, whereas it occurs at 225.4 cm^{-1} for the 2H phase.

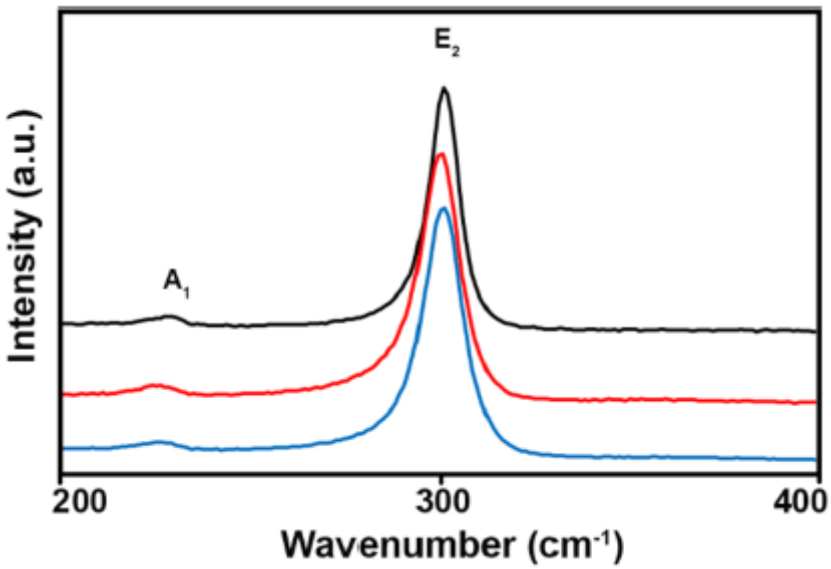

Figure 2.6. (a) Raman spectra of 6R (black), 2H (red), and 1T (blue) germanane products.

About the Thermal Parameters of the 6R Phase the Raman spectra were collected at each temperature for which diffraction was obtained (Figure 2.7). The out-of-plane A_1 vibration located at 227−229 cm−1 and the in-plane E_2 vibration located at 301−304 cm^{-1} both decrease in wavenumber as the temperature of the system is increased (Figure 7d). This relationship is directly correlated to the increase in Ge−Ge and Ge−H bond lengths as the temperature increases. Similar trends are widely observed in other 2D materials such as MoS_2 and phosphorene.[46–48]

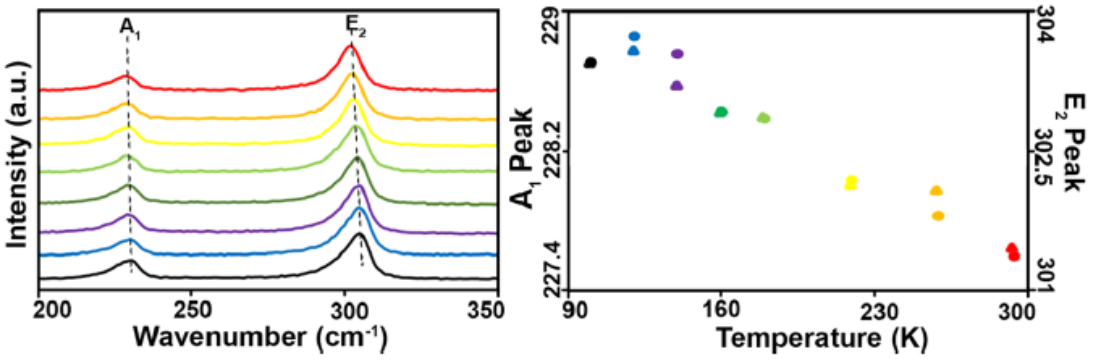

Figure 2.7. Raman spectroscopy data at different temperatures (left). Raman shifts of the A_1 (triangle) and E_2 (circles) modes in the 2H germanane phase. Measurements were carried out at 100 (black), 120 (blue), 140 (purple), 160 (dark green), 180 (light green), 220 (yellow), 260 (orange), and 295 (red) K.

The thermal expansion of the 6R germanane phase was studied along with the temperature dependent Raman spectra. The in-plane lattice constants exhibit a negative thermal expansion, while the out of- plane lattice constants have a positive thermal expansion. The wavenumber of the Raman modes decrease as a function of temperature, common in layered materials.

A comparison and contrast of the Raman spectra of GeH and Ge is shown in Figure 2.8. The main Ge-Ge stretch in GeH occurs at 302 cm^{-1}, which is slightly blue-shifted compared to the 297 cm-1 E_2 Raman mode for crystalline germanium. In addition, a second vibrational mode emerges at 228 cm^{-1}. The symmetries of the vibrational modes are shown in the inset of this figure.

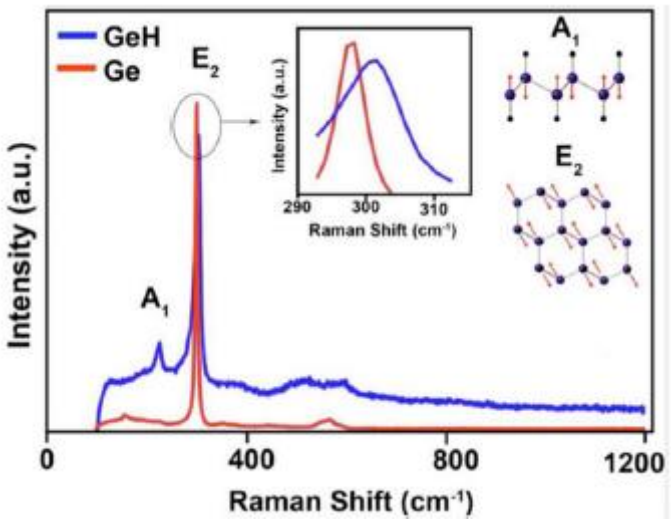

Figure 2. 8 Raman of GeH (blue) and Ge (red). *The middle inset highlights the difference in energy of the E_2 peak between GeH and Ge while the right insets are schematic illustrations of the A_1 and E_2 vibrational modes.*

2.2 Absorption Spectroscopy

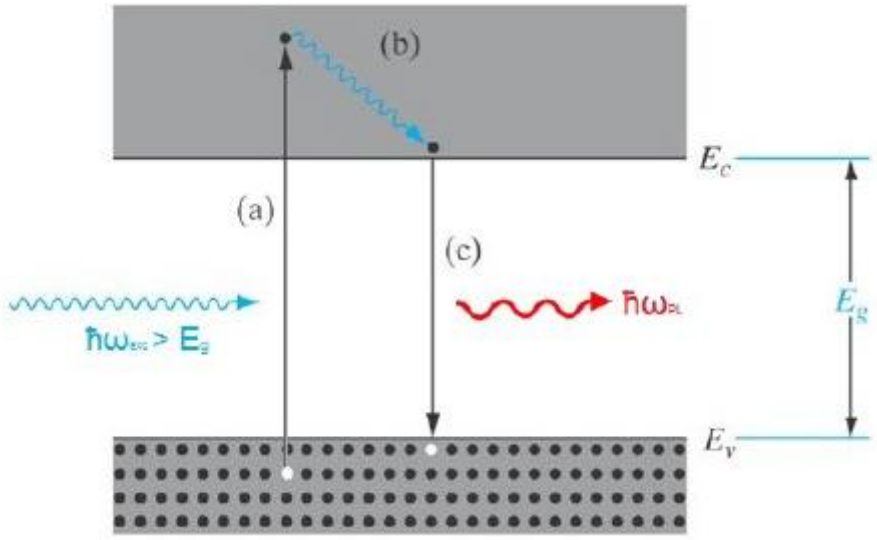

Figure 2.9: Simplified energy diagram illustrating the (a) absorption of a photon with energy greater than the energy gap, (b) thermalization of the electron and (c) re-emission of a photon with energy lower than the absorbed photon. Original image taken from [40].

Absorption spectroscopy is a term describing any spectroscopic technique that measures the absorption of electromagnetic radiation due to its interaction with matter. During an absorption experiment, photons of selected frequencies are directed onto the sample and relative transmission of the various photons is observed.

Figure 2.9 shows a simplified energy diagram of two separate bands in a semiconductor. There are two requirements for transitions of electrons between the valence and the conduction band and vice versa: (a) the energy has to be conserved and (b) the momentum has to be conserved [41]. The law of conservation of energy applied to the interband transition dictates that:

$$E_f = E_i + h \cdot f \quad (2.12)$$

where E_i and E_f is the electron energy in the valence and conduction band, respectively and $h \cdot f$ is the photon energy. It is apparent from Fig. 2.10 that the minimum value of $(E_f - E_i)$ is equal to E_g. This signals that the absorption exhibits a

threshold behavior: the energy of a photon can be transferred to an electron in the valence band and excite it to the conduction band, if the photon energy is larger than the bandgap energy Eg. The photon is absorbed during this process and an electron-hole pair is generated. As the photon energy is reduced below E_g, the crystal becomes transparent to light. Additionally, the existence of a continuous range of energy states within the upper and lower bands implies that the interband transitions will be possible over a continuous range of frequencies, contrary to isolated atoms which exhibit discrete absorption lines.

Conservation of momentum demands that the change in crystal momentum of the electron must equal the momentum of the photon. Due to the negligible photon momentum, this restriction practically requires that the electron wave vector does not change significantly during the absorption process:

$$\mathbf{k_f} \approx \mathbf{k_i} \quad (2.13)$$

$\mathbf{k_i}$, $\mathbf{k_f}$ are the wavevectors of the initial and final electron state. Therefore, photon absorption is represented as a vertical line on E-k diagrams. It is apparent that this second restriction strongly correlates with the bandgap nature of the material. For a direct-gap semiconductor, the fact that the minimum of the conduction band is above the maximum of the valence band readily satisfies Eq. (2.13). On the other hand, band extrema do not coincide in indirect-gap materials. As a result, a phonon is needed for the conservation of the momentum in order to enable the interband transition of an electron from the maximum of the valence band to the minimum of the conduction band. Indirect transitions are characterized as second-order processes as they require three entities to intersect in order to proceed: an electron, a photon and a phonon. Direct interband transition are instead first-order processes since there is no phonon participation. Subsequently, the two-particle process is less probable and has a much smaller transition rate. However, indirect absorption plays a crucial role in technologically important devices such as silicon detectors and solar cells [41-42].

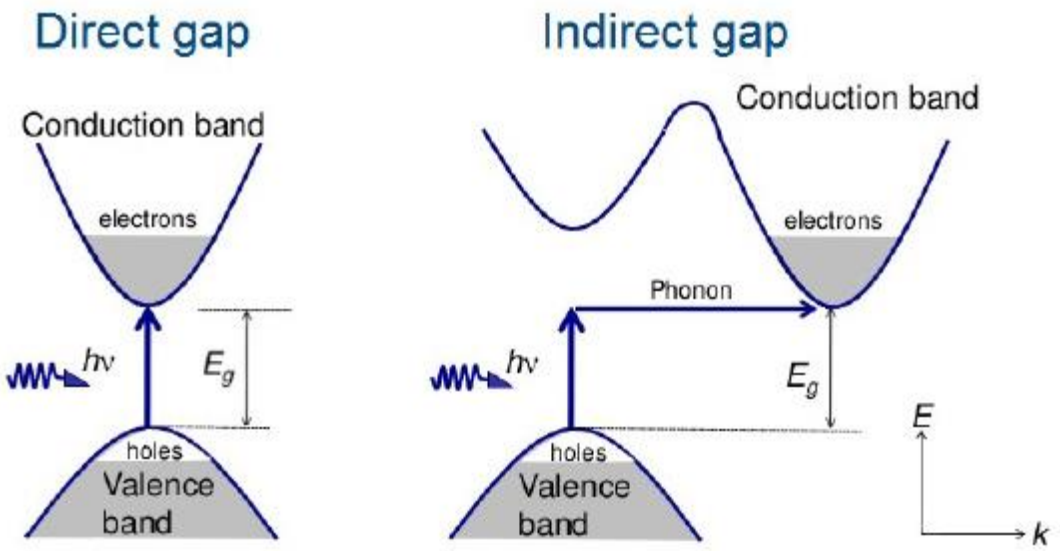

Figure 2.10: Interband absorption in a direct (left) and indirect (right) semiconductor. The grey shading indicates that the energy states are occupied by electrons [43].

Differential reflectance or reflectivity (RC) spectroscopy provides an effective measure of absorbance for ultrathin samples. The fractional change δR for an atomically thin layer relative to the reflectance of a dielectric substrate is directly proportional to the absorbance A of the material according to the following relation:

$$\delta_R(\lambda) = \frac{R_{sub} - R_{sample}}{R_{sub}} = \frac{4}{n_{sub}^2 - 1} * A(\lambda) \quad (2.14)$$

where R_{sample} is the measured reflectance of the material on the substrate, R_{sub} and n_{sub} is the reflectance and refractive index of the underlying substrate, respectively, n_{sub} is assumed to be independent of wavelength in the spectral region of interest. Differential reflectance has been used recently to study the optical properties of 2D materials, especially transition metal dichalcogenides [44-46].

2.3 Photoluminescence Spectroscopy

We have previously considered the case of interband absorption where the semiconductor is excited via the absorption of photons from the applied radiation. The opposite process in which excited electrons drop back to the conduction band by

emitting photons is termed interband luminescence and is the subject of the remaining of this subsection.

In order for a material to emit radiation it has to be properly energized by some external means. Luminescence can be subdivided according to the excitation mechanism: Photoluminescence (PL) is the emission of light by a material that has been previously excited by radiation of higher frequency. Other mechanisms involve the flow of electrical current (electroluminescence), high-energy electron bombardment (cathodoluminescence) etc. but are out of scope for this thesis. The physical process behind photoluminescence mainly involves three separate steps. Initially, electron-hole pairs are injected via the absorption of photons with energy greater than Eg. Afterwards, the photoexcited e-h pairs relax towards lower energy states and reach quasi-thermal equilibrium with the lattice. The excess energy is lost as the carriers collide with lattice vibrations before residing close to band extrema energies, Ec and Ev; this process is referred to as thermalization. In the final step, radiative recombination of electron-hole pairs occurs as an electron drops to an empty state in the valence band, giving off a photon of approximately the band gap energy. These steps are schematically illustrated in the simplified diagram of Fig. 2.10. The electron-phonon coupling is most solids is very strong and electron-hole pairs thermalize on time scales as short as ~100 fs. Radiative lifetimes are in the nanosecond range, therefore carriers are able to relax by phonon emission before recombination. Under special circumstances, hot luminescence, i.e. emission from incompletely thermalized e-h pairs can be observed [41-42,46].

However, charge carriers may potentially recombine without the emission of light. In real life applications, materials contain defect levels within the bandgap perhaps due to intentional or unintentional doping agents or crystal defects and dislocations. These energy levels have a strong tendency to temporarily capture carriers as an intermediate step prior to the completion of the recombination process; a carrier is first captured at this energy level and then makes an annihilating transition to the opposite band. The excess energy is released as thermal energy (heat), or equivalently, phonons are produced. Additionally, during an Auger type process, excess energy can be transferred to a third carrier who is then excited to higher energy levels within its respective band. This highly energetic carrier then thermalizes back down to the band edge, through collisions with the semiconductor lattice. The

previously described non-radiative processes compete with radiative recombination and if they occur with a faster rate than radiative transitions, very little light will be eventually emitted.

Even though the previous analysis qualitatively describes the mechanism of interband photoluminescence, the distinction between direct and indirect bandgap semiconductors is again necessary. Figure 2.11 shows the E-k diagram for interband absorption and photoluminescence in a direct and indirect semiconductor. The thermalization process is not shown, only that electrons accumulate at the bottom of the conduction band and holes at the top of the valence band. In the direct semiconductor, little change in momentum is required for the recombination. The conservation of both energy and momentum is satisfied simply by the emission of a photon which is presented as a vertical downward arrow. The luminescence efficiency is therefore expected to be high. In an indirect gap material, the emission of a photon will conserve energy but not momentum. Thus, for the recombination process to proceed, a phonon must either be emitted or absorbed

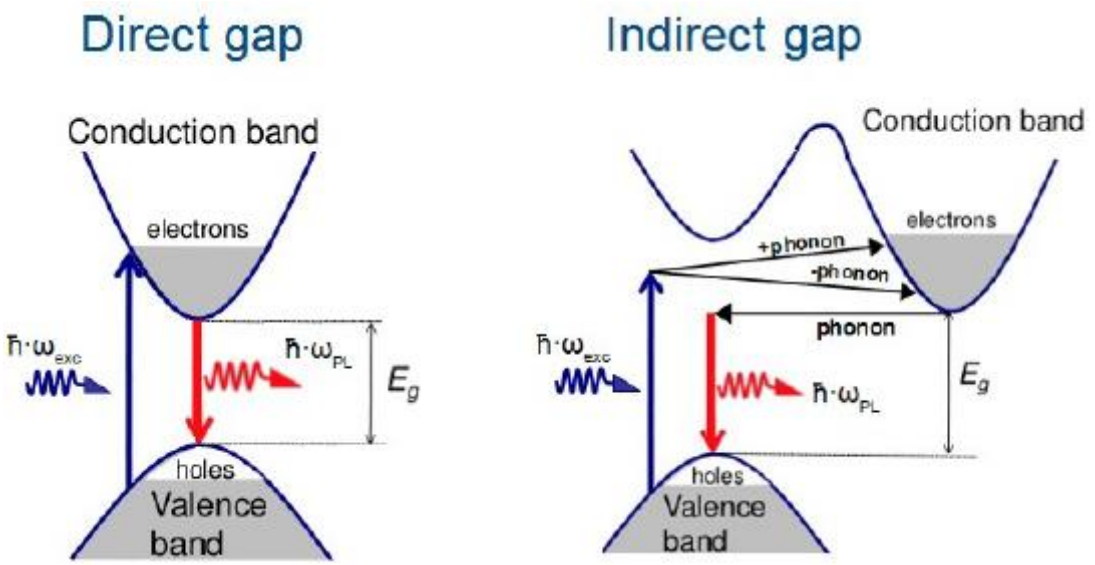

Figure 2.11: Schematic band diagrams for interband absorption and luminescence in a direct (left) and indirect (right) semiconductor. For the indirect light emission, phonon absorption and emission are represented by a horizontal arrow [43].

coincident with emission of a photon. This requirement constitutes indirect interband recombination as a second-order process with diminished recombination rate. The

competition with non-radiative recombination leads to a weak luminescence efficiency [41-42, 46].

Photoluminescence spectroscopy is a powerful, non-contact, nondestructive optical method for material characterization. In semiconductor research, it is a widely employed diagnostic and development tool for obtaining information regarding band structure, impurity and defect levels and other carrier-related phenomena such as transport, relaxation, recombination and exciton formation. At room temperature, PL emission is usually broad in width and its intensity is thermally quenched. When samples are cooled to cryogenic temperatures, structural details may be resolved, allowing the study of fundamental properties of semiconductors. Additionally, by quantifying the amount of radiative recombination in comparison with non-radiative recombination, material quality can be assessed [47-48]. The usual goal is the development of light-emitting devices based on electroluminescence. Usually, this goal is realized after the emission mechanisms have been thoroughly studied using photoluminescence spectroscopy and its variations [41].

2.3.1 Photoluminescence and XRD Spectroscopy of bulk GeH

To determine the effect of the transfer on the quality of GeH films, a series of characterization measurements were performed before and after transferring in substrates from the synthesis method which used in literature. To minimize substrate-related effects, they transfer the GeH film from its original Ge(111) substrate to another Ge(111) substrate. The out-of-plane lattice spacing was analyzed using XRD on a 600 nm (∼1000 layers) GeH film. Before transfer, it has observe a peak at $2\theta = 15.8°$ which corresponds to the GeH layer spacing of 5.7 Å. This is in agreement with XRD characterizations of bulk GeH crystals, where synchrotron- based measurements of the pair distribution function have confirmed the buckled honeycomb structure of the GeH layers [10]. As shown in figure 2.12(d), the position and line width of the GeH peak are preserved after transfer, indicating that the transfer does not produce major changes to the crystal structure.

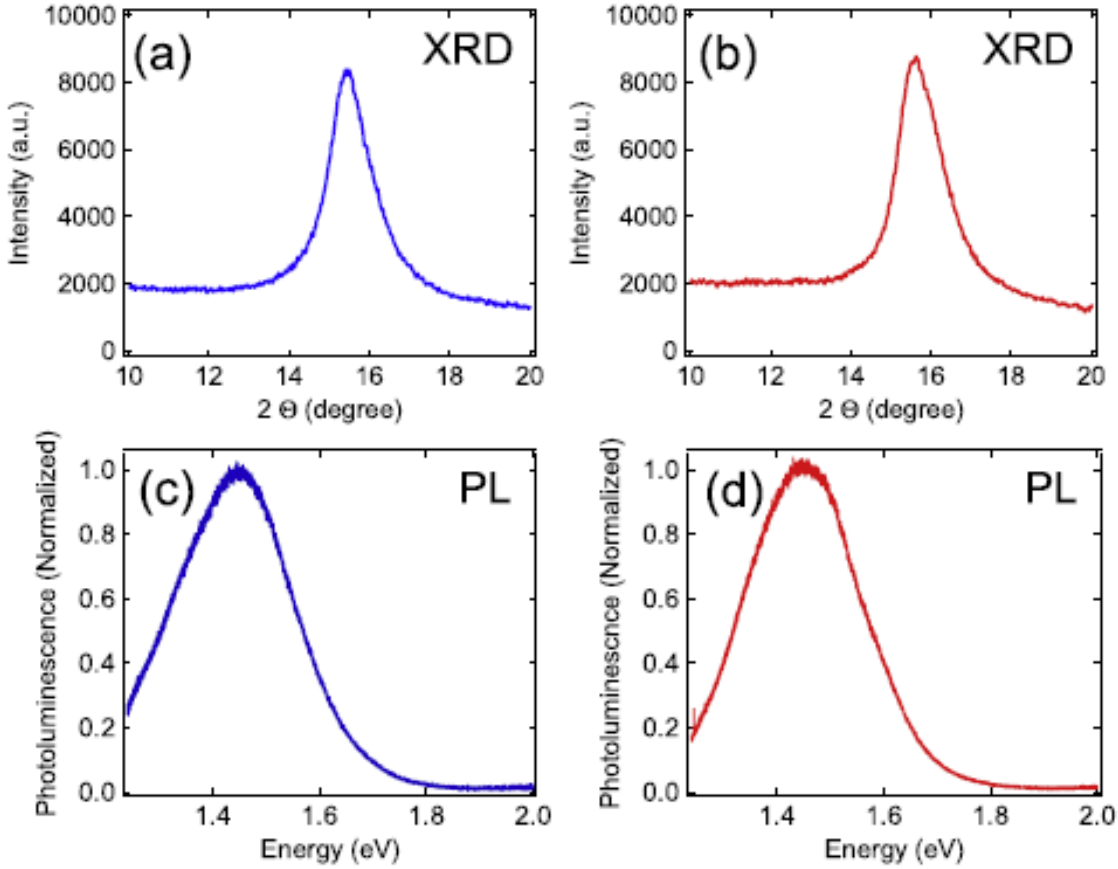

Figure 2.12.(a)XRD of as-grown 600 nm(~1000 layers) GeH film, (b)XRDof transferred 600 nm(~1000 layers) GeH film, (c) PL of as-grown 600 nm(~1000 layers) GeH film, (d) PL of transferred 600 nm(~1000 layers) GeH film.

The PL spectrum before transfer exhibits a peak at ~1.45 eV, (figure 2.12c) which is consistent with previous reports of PL on epitaxial GeH [22]. After transfer, the PL spectrum again exhibits a peak at ~1.45 eV and the intensity is not degraded (figure 2.12d). Notably, they did not observe PL at ~1.9 eV, which is reported to occur in the presence of oxidation [22]. This suggests that the transfer of GeH does not promote oxidation and preserves the optical quality.

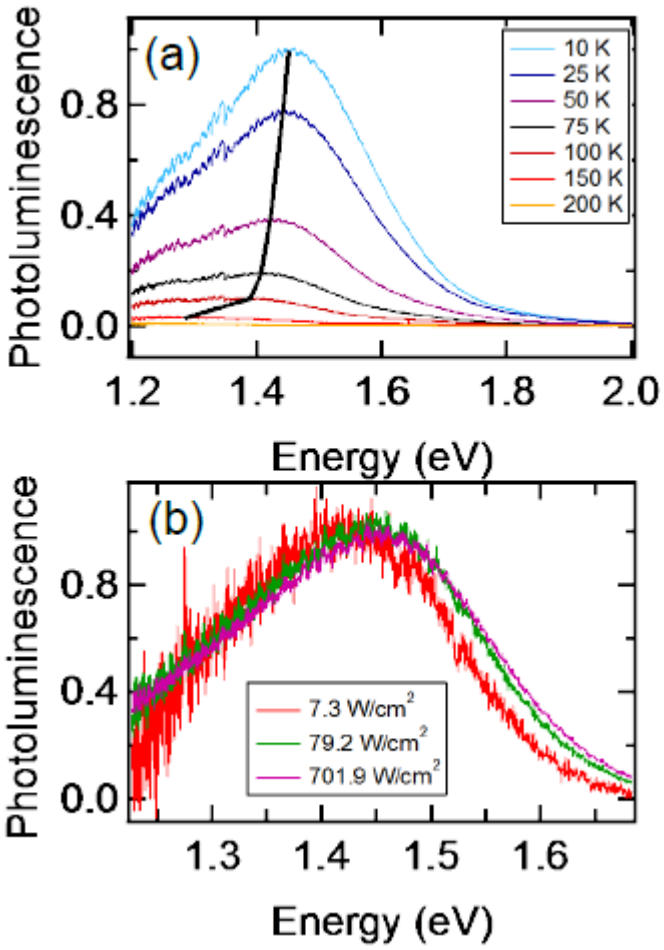

Figure 2.13: (a) Temperature dependent PL of a 600 nm germanane sample. The black lines indicate the shift in peak center with temperature (b) Normalized power dependent PL showing and broadening and shift to higher energy with increasing excitation intensity

Part II:

Experimental Methods and Results

Experimental Methods 3

3.1 Preparation and optical identification of GeH

Bulk and monolayer synthesis constitutes the starting point for almost any type of research on 2D materials. Two- dimensional group IV elements like germanane and graphane can be synthesized using various methods which can be divided into two categories: the top-down approach, where the bulk crystals are exfoliated into either few-layer or monolayer structures, and the bottom-up approach using growth methods such as Chemical Vapor Deposition (CVD) or epitaxial growth techniques such as drop casting method.

The drop casting method is very simple to conduct the experiments. Regarding the procedure, we place a quantity of powder produced by the University of Ioannina (more specifically by the doctoral students Nikolaos Chalmpes and Theodosis Giousis under the supervision of Prof. Dimitrios Gournis) in a vial and add a specific amount of solvent in it. Then, we perform an ultrasonication procedure for 10 minutes with the aid of a syringe and place several drops onto Silicon/Silicon Oxide (Si/SiO_2). We finally leave these substrates under the suction for the solvent to evaporate and the samples to dry.

Generally, it is desirable to use solvents that are volatile, wet the substrate, and are not susceptible to thin film instabilities (de-wetting). Water tends to be a poor solvent for drop-casting due to the low vapor pressure and large surface tension. In some cases alcohols can be in place of water, while organic solvents (such as hexane, toluene or halogenated solvents) are often very good choices for nanoparticles with hydrophobic capping ligands. During this thesis Dimethylformamide (C_3H_7NO) was used for experiments.

One drawback of drop-casting is that even under near ideal conditions, differences in evaporation rates across the substrate or concentration fluctuations can lead to variations in film thickness or internal structure. However, drop-casting does serve a quick and accessible method for generating thin films on relatively small substrates.

The next step is identifying candidate bulk crystal region and it is usually performed via optical imaging means. It has been found that with an optimal oxide thickness, the presence of bulk film can produce a detectable contrast with respect to the interference color of the underlying oxide layers. This contrast can be observed through an optical microscope and therefore, optical imaging can be used as a rapid, non-invasive and low cost method for the identification of dichalcogenide nanosheets [49]. During this thesis, GeH bulk crystals were deposited on a Si/SiO_2 substrate with a 290 nm oxide thickness.

3.2 Atomic Force Microscopy (AFM)

A Scanning Probe Microscope (SPM) is an instrument used for studying surfaces at the nanoscale level. Images of surfaces are formed by using a physical probe that scans the specimen. The SPM originated with the invention of the Scanning Tunneling Microscope (STM) which is based on applying a tunneling current between the conducting probe tip and a conductive sample in a vacuum state. The Atomic Force Microscope (AFM) was developed to overcome a basic drawback of STM; it can only image conducting or semiconducting surfaces. The AFM has the advantage of imaging almost any type of surface, but also it can measure various physical, chemical, mechanical, electrical and magnetic properties of sample's surface.

The next figure schematically shows the operation principle of atomic force microscopy. The sharp tip (probe) is fixed to the free end of a cantilever. The cantilever and the tip are usually made from Silicon or Silicon Nitride, and are manufactured using micro-machining techniques. AFM relies on the force/interaction between the atoms of the tip and those at the sample's surface, which can be either attractive or repulsive depending on the distance between them. This force can be detected by monitoring how much the cantilever deflects as it scans the surface of the sample. The deflection of the cantilever can be quantified by the measurement of a laser beam that is reflected off the backside of the cantilever and directed onto a Position Sensitive Photodetector (PSPD). The tube-shaped scanner located under the sample can move a sample both in the horizontal (XY) and in the vertical direction (Z). It repetitively scans the sample line by line, while the PSPD signal is used to

establish a feedback loop which controls the vertical movement of the scanner as the cantilever moves across the sample surface [50].

All measurements during this thesis were carried out with a Park XE7 AFM system that utilizes the so-called "Tapping mode" of operation [50-51]. Tapping mode imaging is implemented by oscillating the cantilever in free-space in the vicinity of its resonance frequency. The frequency and amplitude of the driving signal are kept constant by a feedback circuit, resulting in a constant amplitude of the cantilever oscillation provided that there is no drift or interaction with the surface. As the vibrating cantilever gets close to the sample, it taps its surface repeatedly. The force gradient between tip and sample causes the resonant frequency of cantilever to shift. Attractive forces will shift the cantilever resonant frequency to lower values, whereas repulsive forces will shift the cantilever resonant frequency higher. The oscillation is also damped when the tip is closer to the surface.

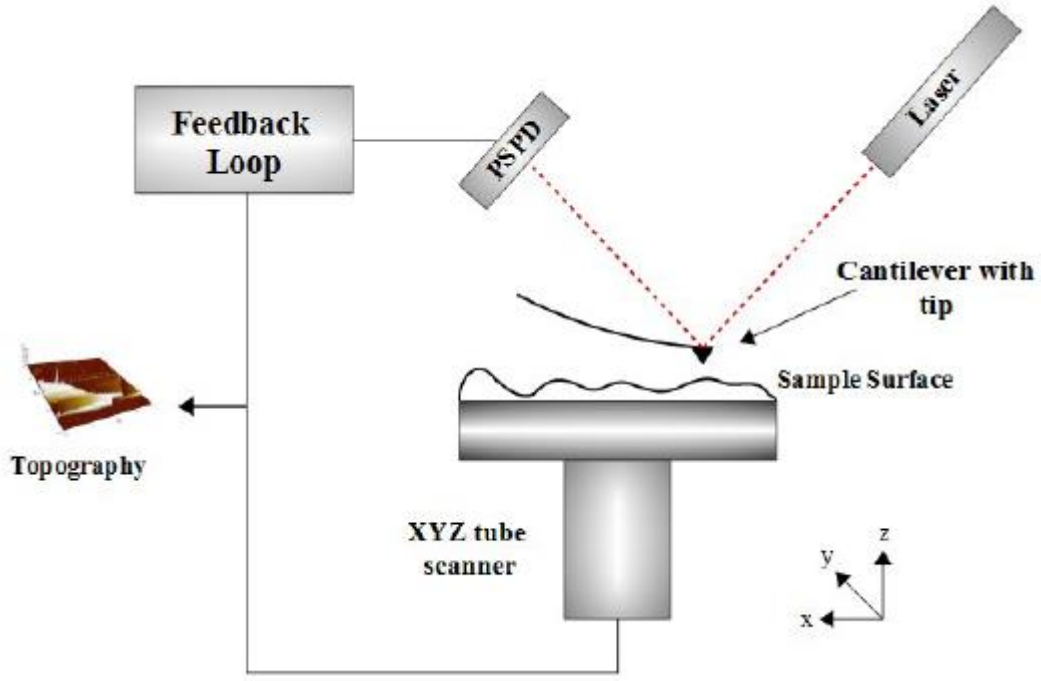

Figure 3.1: Schematic illustration of conventional AFM scanning.

This change in amplitude is used to identify and measure surface features, while being the parameter that goes into the feedback circuit that controls the height of the

cantilever above the sample. The feedback circuit adjusts the height to maintain a fixed cantilever oscillation amplitude as the cantilever is scanned over the sample. This method, keeping intermittent contact between the sample surface and the vibrating cantilever is called Taping mode. Each sample area is measured with 256x256 pixels (data points) and a frequency of 0.5 Hz.

3.3 Experimental Setup of Raman Spectrometry

Modern micro-Raman (μ-Raman) instrumentation is based on three primary components: a laser as the excitation source, a spectrometer as the detector and a microscope as a sampling apparatus. By coupling a visible spectrometer to a microscope, Raman analysis with a microscopic laser spot (of the order of 0.5-10 μm) is achieved. However, simply adding a microscope assists in giving lateral (XY axes) spatial resolution, but does not give depth (Z axis) spatial resolution. For this purpose, confocal optics are required [52].

Figure 3.2 schematically depicts a generic confocal Raman setup. The laser beam firstly passes through a beam splitter and then is focused onto the sample by an objective lens. Scattered radiation is collected from the microscope through the objective and hits the beam splitter which now acts as a mirror. A filter is placed to remove the much more intense Rayleigh scattering which could potentially damage the light detector. If only Stokes (anti-Stokes) scattering is to be measured, a long (short) pass filter with a sharp edge close to the wavelength of the laser can be used. If instead we wish to measure both the Stokes and anti-Stokes radiation, a notch filter should be employed to block only a narrow band about the laser wavelength. After the filter, the radiation is arranged to pass through a pinhole aperture (25 to 100 μm in diameter) which rejects signals that are not in the focal plane of the objective. Consequently, the out-of-focus background (substrate) signals can be effectively reduced and it is possible to measure the Raman spectrum of a sample at different depth by moving the focal plane in the Z direction. The in-focus scattered light enters a spectrometer where is being spectrally dispersed by a diffraction grating. Finally,

the dispersed light is projected onto a Charged Coupled Device (CCD), a silicon-based semiconductor arranged as an array of photosensitive elements. The incoming photons are converted into an electrical signal which then is turned into a digital signal. The result is a spectrum with a number of counts assigned to each resolvable energy. The Raman scattering is collected in the so-called back-scattering geometry since the laser beam is focused onto the sample with an objective lens and the scattered light is collected with the same objective [32-33].

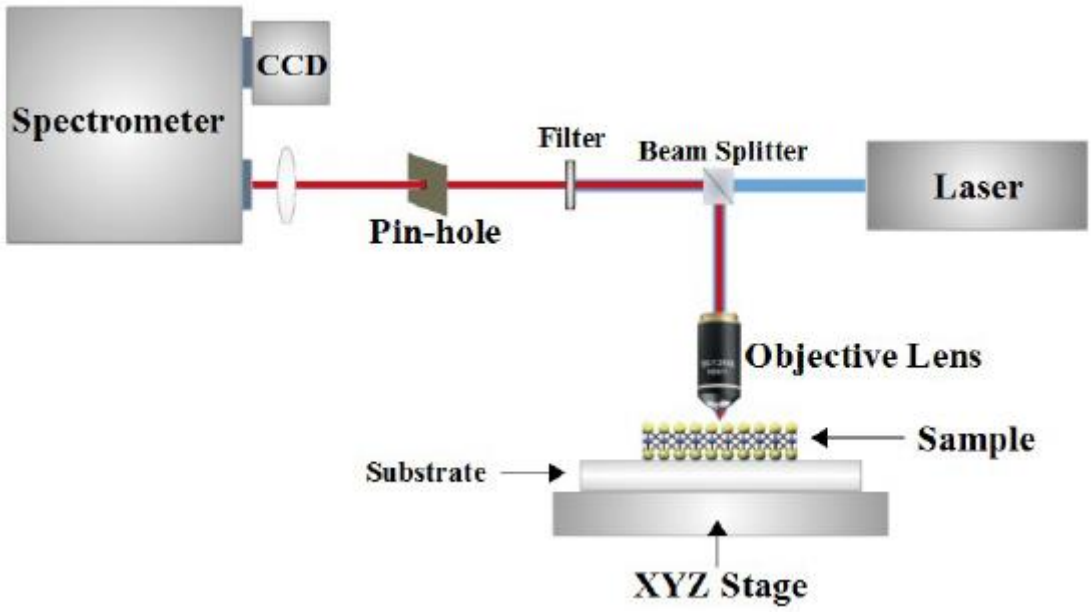

Figure 3.2: Schematic illustration of a confocal micro-Raman Spectrometer.

All the Raman spectra presented in this thesis have been measured by a Thermo Scientific, Nicolet Almega XR Micro Raman analysis system. It consists of a confocal single monochromator spectrometer which is interfaced with the microscope entirely using high-throughput, free-space optics. It is equipped with three microscopy objective lenses, a scanning motorized XYZ stage and a 780 nm diode-pumped solid-state laser (DPSS) with maximum output power of 50 mW. The power of the incident beam is controlled with a neutral density filter and a high-resolution grating (2400 grooves/mm) analyses the signal. A 100 μm pinhole is used as the confocal aperture.

A 100x lens with a numerical aperture of 0.90 is used in all measurements, yielding a spot diameter of 0.9 μm [53].

3.4 Optical setup of Photoluminescence and Reflectivity Spectroscopy

During the period of this master thesis, an optical setup has been developed at the Ultrafast Laser Micro/Nano Processing Lab (ULMNP) of the Institute of electronic Structure and Laser (IESL) at the Foundation for Research and Technology-Hellas (FORTH). All the micro-photoluminescence (μPL), as well as the micro-differential reflectance (μΔR) that will be presented in chapter IV, were carried out with this custom optical setup. A picture of the custom configuration is shown in Fig. 3.3.

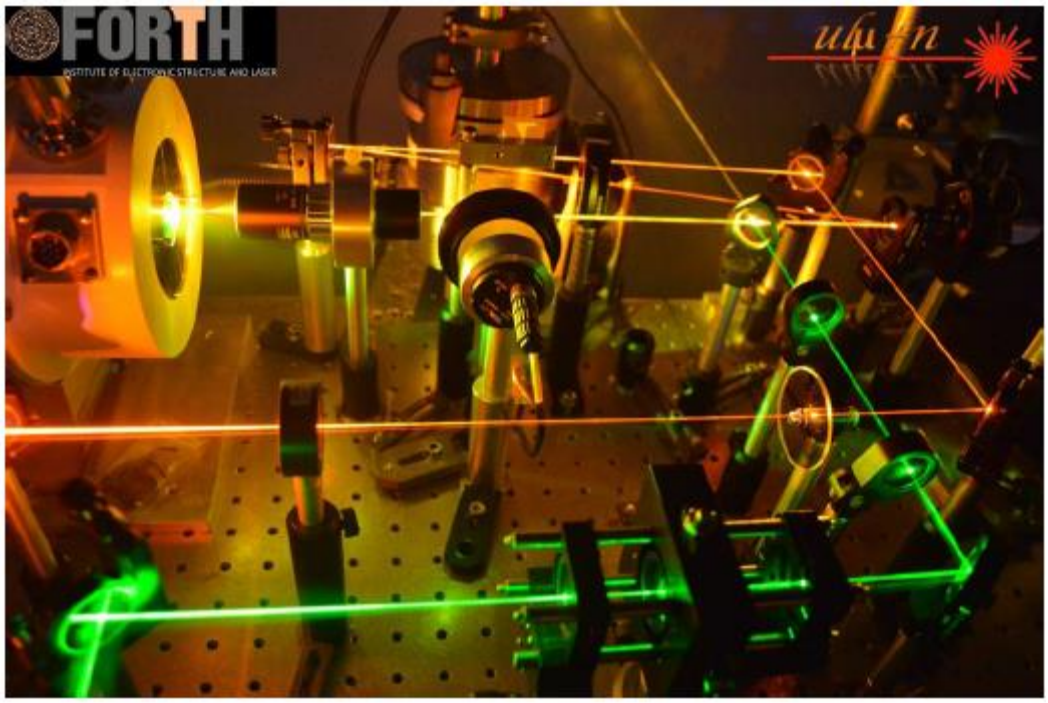

Fig. 3.3: Picture of the custom optical setup developed at the ULMNP lab of IESL/FORTH.

A detailed discussion of the different configurations (μPL and μΔR) that consist the complete optical system will be presented separately in the following subchapters. Also, an individual subchapter will focus on the cryogenic system design.

An iHR-320 spectrometer (Horiba Scientific/Jobin Yvon Technology) was used in this setup (Fig.3.4a). It is an automated spectrometer with a 320mm focal length (*f*/4.1 aperture) and offers two different gratings on its turret: 300g/mm and 1200g/mm. The wavelength range is 150nm-15μm (1200g/mm) and the resolution with the 1200g/mm is 0.06nm (measured at 435nm). A top-view schematic representation of the iHR-320 showing the slits and its focal plane is shown in Fig. 3.4b. The wavelength accuracy is ±0.20nm and the spectral dispersion 2.35nm/mm. The step size of the automated turret is 0.002nm.

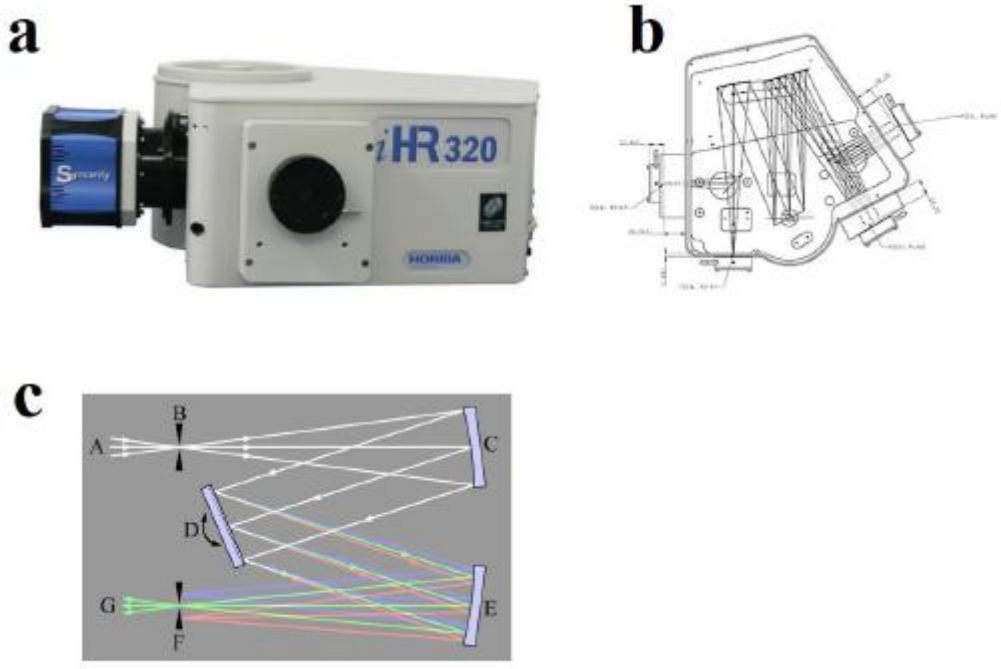

Fig. 3.4: a) Picture of the iHR-320 spectrometer. b) iHR-320 top view, showing slits and focal plane. c) Schematic representation of a Czerny-Turner monochromator.

The geometry of the monochromator used in the setup is shown in Fig. 3.4c. It is a common Czerny–Turner design, where the incoming signal (A) is focused is at the entrance slit (B). The slit is placed at the focal point of a parabolic mirror (C) that

collimates the divergent incoming light (focused at infinity). The collimated light is then diffracted from a reflective grating (D) and is collected by a second parabolic mirror (E), which refocuses the dispersed light on the exit slit (F). Since after the grating the different wavelengths are spread out, they arrive at a separate point in the exit-slit plane. A rotation of the reflective grating causes the band of wavelengths to move relative to the exit slit, so that the desired entrance slit signal is centered on the exit slit.

A Syncerity multichannel charge-coupled device (CCD) Deep Cooled Camera (Fig. 3.4a) is attached to the exit of the monochromator. It utilizes the thermoelectric effect to operate at -600C for high signal-to-noise ratio. The CCD sensor contains 1024×256 pixels with a pixel size of 26μm×26μm. The spectral range is 250nm-1050nm with a quantum efficiency of almost 60% at 750nm.

3.4.1 micro-Photoluminescence configuration

Micro-Photoluminescence (μ-PL) spectroscopy is largely based on the same primary experimental components as μ-Raman. Therefore, if certain experimental conditions are met, the two techniques could potentially be combined on a single microscope system. Figure 3.5 illustrates the experimental setup used during this thesis. Samples were mounted on a continuous flow cryostat which facilitates cryogenic to room temperature measurements as well as vacuum (< 0.2 Pa) conditions.

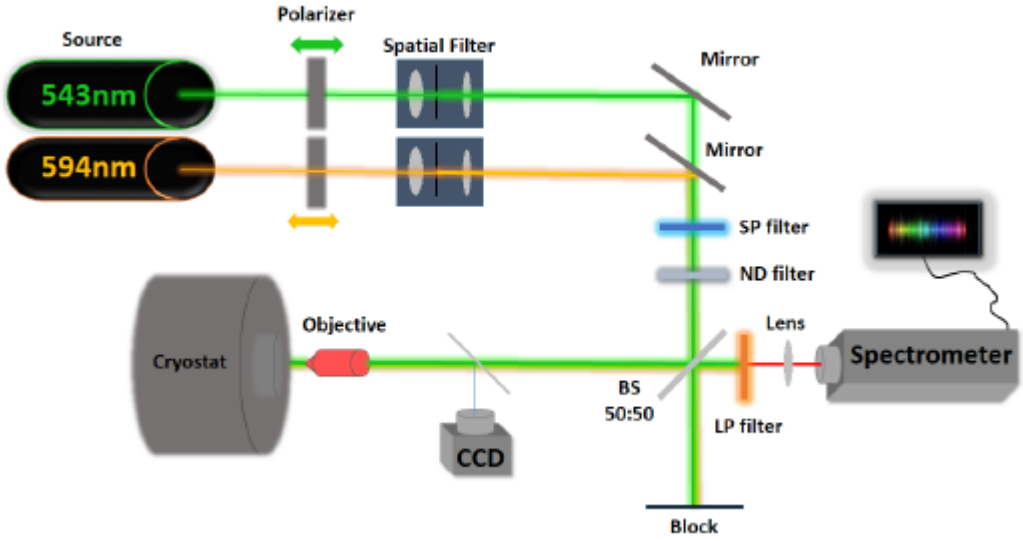

Fig. 3.5: *Schematic representation of the μPL configuration.*

Two different excitation sources were placed in this setup: a) continuous wave (CW) He-Ne 543nm (photon energy: 2.28eV) and b) He-Ne 594nm (photon energy: 2.09eV). In this thesis the 543nm laser excitation was used. The laser beam is *s*-polarized and passes through a spatial filter (KT310, Thorlabs) for two reasons: the first is to clean the Gaussian beam from its spatially varying intensity noise and acquire a uniform energy distribution. The second is to expand the beam size in order to fit through the aperture of the objective and achieve diffraction limited spot size. After the spatial filter, the beam passes through a short pass (SP) filter (FESH550, Thorlabs) to reduce the noise at higher wavelengths. The power of the laser beam is controlled via a neutral density (ND) filter (0-2 OD, NE520B-A, Thorlabs). A 50:50 beam splitter (BS 50:50, BSW10, Thorlabs) is used to reflect and drive the beam to the objective lens. A Mitutoyo 50x (NA:0.42, *f*=200mm) focuses the spot size down to ~1μm on the sample which is placed inside a cryostat (ST500, Jannis). The position of the sample is controlled with a XYZ mechanical translation stage (PT3, Thorlabs) and the excitation procedure is continuously monitored and controlled via a CCD optical setup. Following the excitation, the emitted PL signal passes through a long pass (LP) filter (FELH550, Thorlabs) to eliminate the emission of the laser.

3.4.2 micro Reflectance configuration

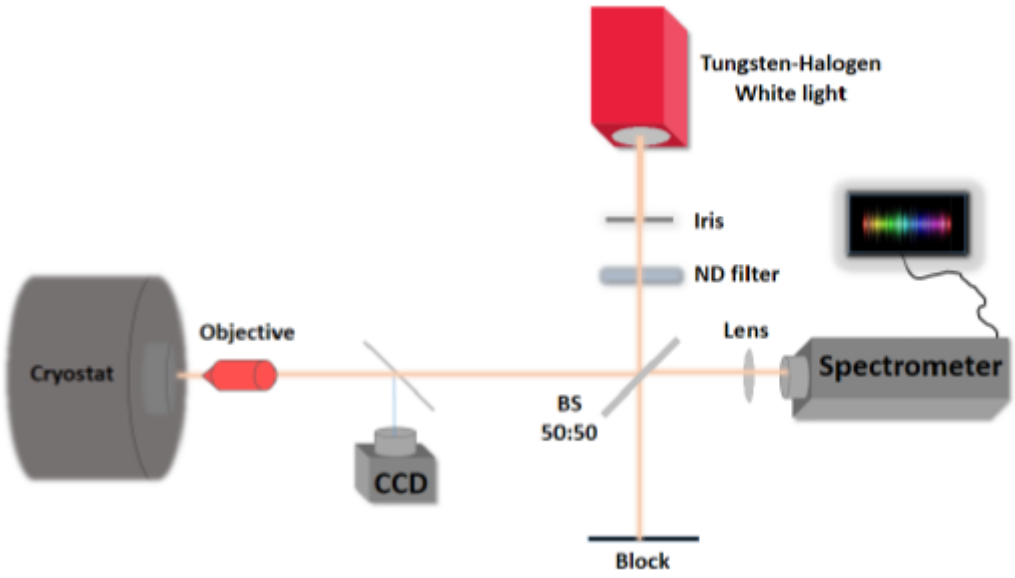

Fig. 3.6: Schematic representation of the μDifferential Reflectance configuration

The same optical setup can be easily modified by flipping the mirrors of the μPL configuration and permit the aligned super continuum light (360nm - 2600nm) of a stabilized tungsten-halogen source (SL201L, Thorlabs) to pass through an iris and follow the same optical path as discussed in section 3.4.1. It is apparent that in order to perform a differential reflectance experiment in the same optical path, the long and short pass filters must be first removed in order to exploit the spectrum of the super continuum efficiently (Fig. 3.6). The diameter of the white light spot size on the sample is approximately 3μm. In a typical experiment, the electronic transitions of a very thin film are probed with the broad-band light and the reflected signal that follows the backscattering geometry is measured. However, because the flakes are atomically thick and placed on SiO_2/Si substrate, the reflected light spectra include the illumination source profile, the sample transmission and absorption, the substrate reflection and absorption, and resonant effects due to the thickness of the SiO_2. To reveal the contribution from the bulk germanane flake, we take theRatio between the

intensity measured from the flake, *Ion*, and from the substrate (just off the flake), $\Delta R = \frac{I_{on}}{I_{off}}$.

Experimental Results and Discussion 4

4.1 Bulk crystal Identification

After performing exfoliation onto a silicon wafer covered with 290 nm of SiO_2, candidate bulk crystals are reliably identified under a microscope by their optical contrast. Figure 4.1a illustrates an optical microscopy image of a drop casting exfoliated GeH bulk crystal. The bulk crystals appear as light-yellow regions which contrast with the brown color of the substrate. As the thickness decreases, the color changes from light-yellow, for the bulk to purple for the multilayer and few layer crystals. AFM imaging indicates that the sample has a thickness of ~ 500μm (See Figure 4.1b). This value is consistent with the reported thickness for drop casting exfoliated GeH bulk crystal [9], confirming that a bulk layer is successfully isolated. The lateral dimensions of samples can also be evaluated via AFM measurements.

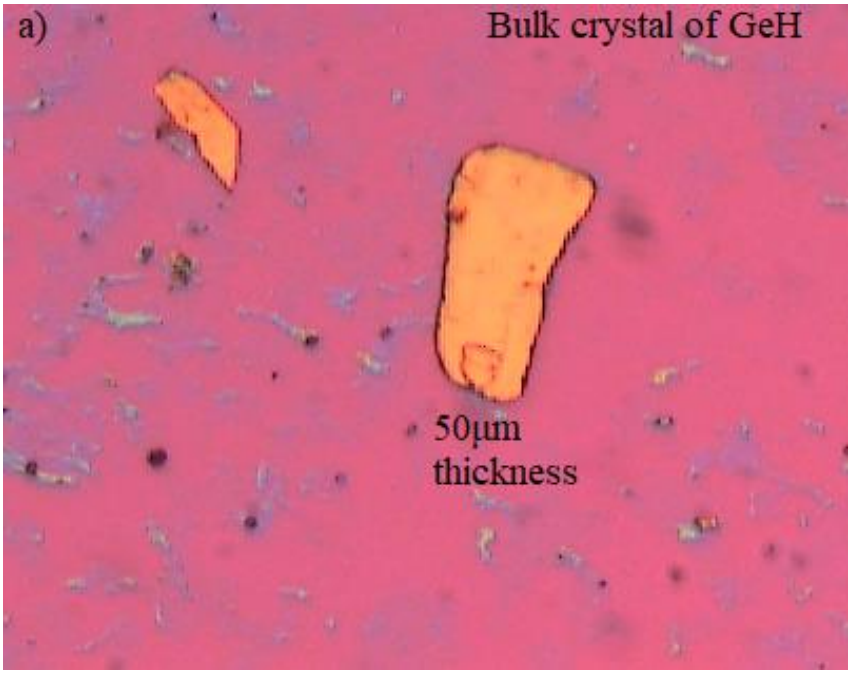

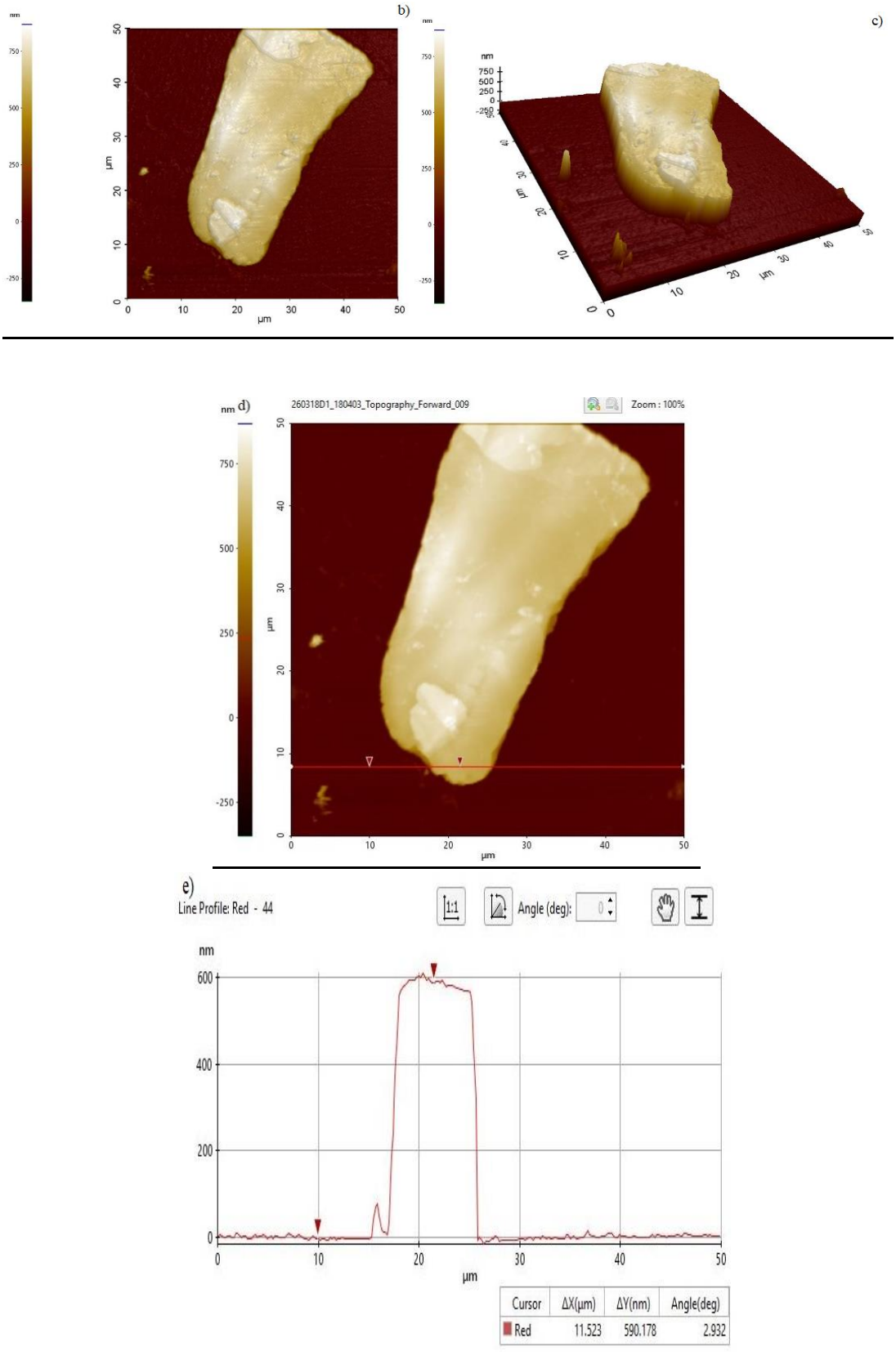

Figure 4.1: a) Optical microscope image of a bulk crystal GeH, b) AFM image of the bulk sample (top view) c) AFM image of the bulk crystal sample (side view), d,e) AFM thickness measurement along thered line.

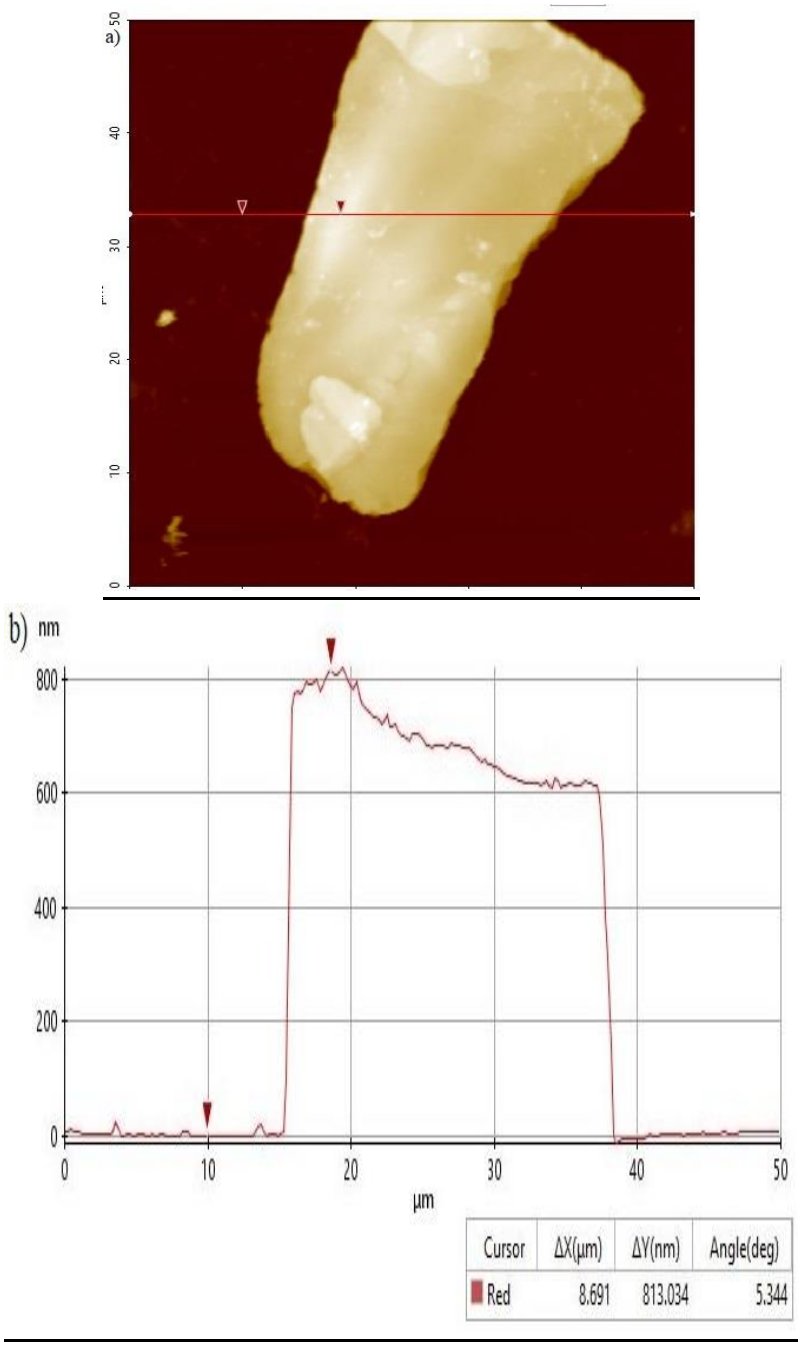

Figure 4.2: a,b) AFM thickness measurement along the red line in comparison with measurement from 4.1 d),e).

The 2D and 3D AFM topography images of the bulk crystal (Figures 4.1 and 4.2) reveal that the sample surface is highly inhomogeneous and the thickness varies considerably across the sample. . The interaction with a dirty cantilever tip or the presence of atmospheric dust can lead to small thickness variations but they cannot

account for the large variations we measure. This could be attributed mainly to the technique used to prepare the crystals. It is well known that the drop-casting method leads to non-uniform crystals with large variation in thickness

4.1.1 Raman spectroscopy of GeH

Micro-Raman Spectroscopy is employed to characterize the samples prepared by the drop-casting method. The Raman spectrum of bulk-GeH under 780 nm excitation wavelength is shown if Figure 4.3. The laser power is kept relatively low (~ 1 mW) in order to avoid structural damage and local heating effects. The out-of-plane A_{1g} and the degenerate in-plane E_{2g} vibrational modes are observed at 228 cm^{-1}, and 302 cm^{-1}, respectively. The intensity of the in plane mode is almost 20 times higher than the corresponding one of the out of plane mode.

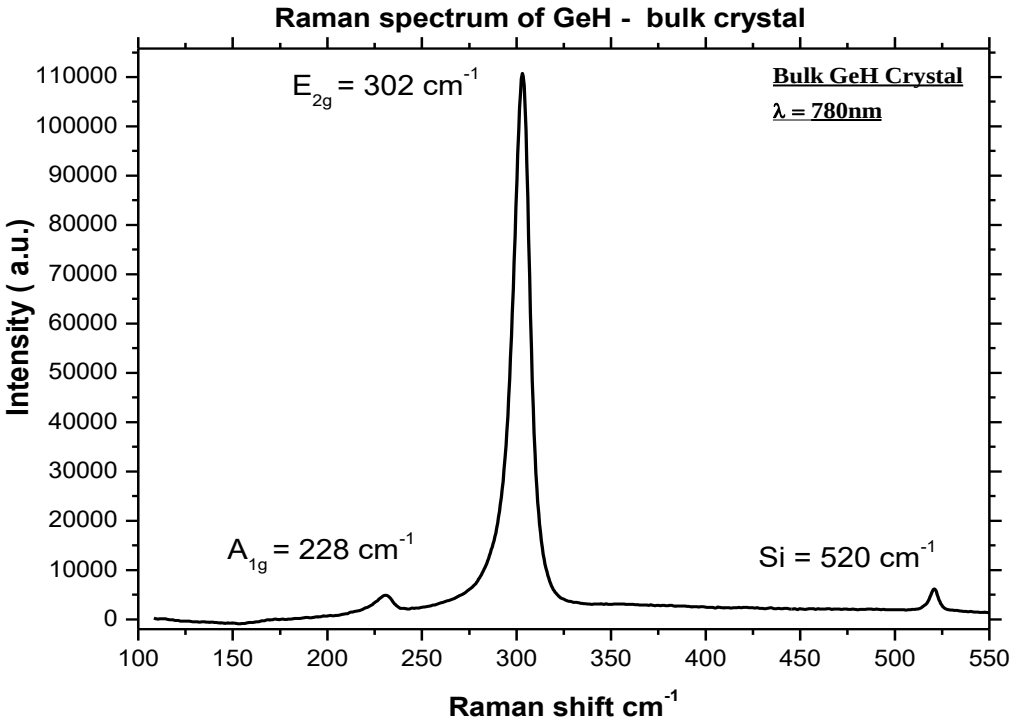

Figure 4.3: Raman spectrum of bulk under 780 nm excitation in the range 100-550 cm^{-1}.

In order to check the uniformity, we performed Raman measurements at different points of the same sample using the same laser line of 780nm (Fig.4.4). We plot the energy position and the intensity of the two main modes in Fig.4.5 (left panel)

and Fig.4.5 (right panel) respectively. There is no appreciable energy shift for both modes and we only observe some variations in the intensity of the in plane mode at different parts of the sample. This is indicative of the non-uniformity in the thickness that we have discussed earlier.

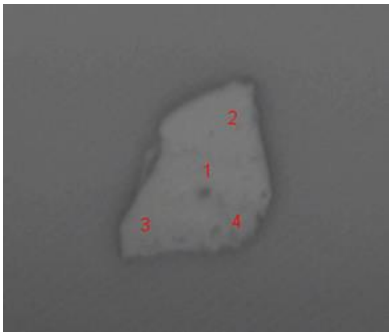

Figure 4.4: Position on the sample where Raman spectra were taken

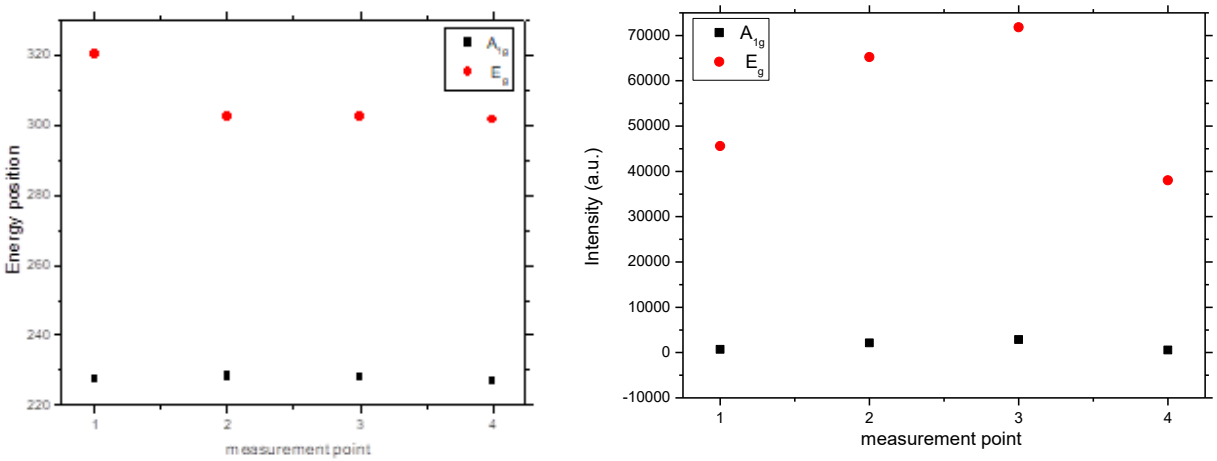

Figure 4.5: Energy position (left) and intensity (right) for the two main vibrational modes, A_{1g} and E_{2g} for the 4 different points on the sample.

Then we changed the laser line to 473nm and we performed Raman spectroscopy on the same sample that initially we acquired spectra with the 780 nm laser line. Again, we kept the laser power densities to very low levels in order to avoid any damage of the sample. In Fig.4.6a, for a comparison, we show the spectrum taken with the 780nm line (the inset shows an optical image of the sample). Fig.4.6b shows

the Raman spectrum taken with the 473nm laser at the same spot on the sample as the 780nm line. There is a dramatic change of the spectrum. The out of plane mode A_{1g} at 228 cm^{-1} is not present while the in-plane mode E_{2g} is now at 292.5 cm^{-1}. From the optical image of the sample in the inset, it is clear this laser line has modified the surface of the sample creating a spot. To check if the changes are permanent, we return to the higher wavelength 780nm laser line and record the spectrum. Fig.4.6c shows that there is no reversibility and the changes on the sample are permanent. If we now choose a different point on the sample that was not exposed to 473nm line, the spectrum looks again exactly like the one in Fig.4.6a. This implies that the damages caused by the 473nm line are really localized to the exposed area. We could understand this behavior by the fact that the energy of the short wavelength excitation is mainly absorbed at the surface causing a local heating that could break some Ge-H bonds and modifying the Raman modes. The absence of the Si Raman peak at 520 cm-1 in Fig.4.6b supports the point that the 473nm line does not reach the substrate and excites only the germanane sample. Peaks ranging from 301cm^{-1} to 289 cm^{-1} indicate the presence of other Ge particulates, which are a byproduct of the GeH synthesis [54].

Initially, we made a measurement using the 780nm wavelength and we radiated our sample with 473nm wavelength. It was maintained that there was a damage threshold of the surface during irradiation despite the smaller laser energy and only one peak appeared in the 289 – 293cm^{-1}.

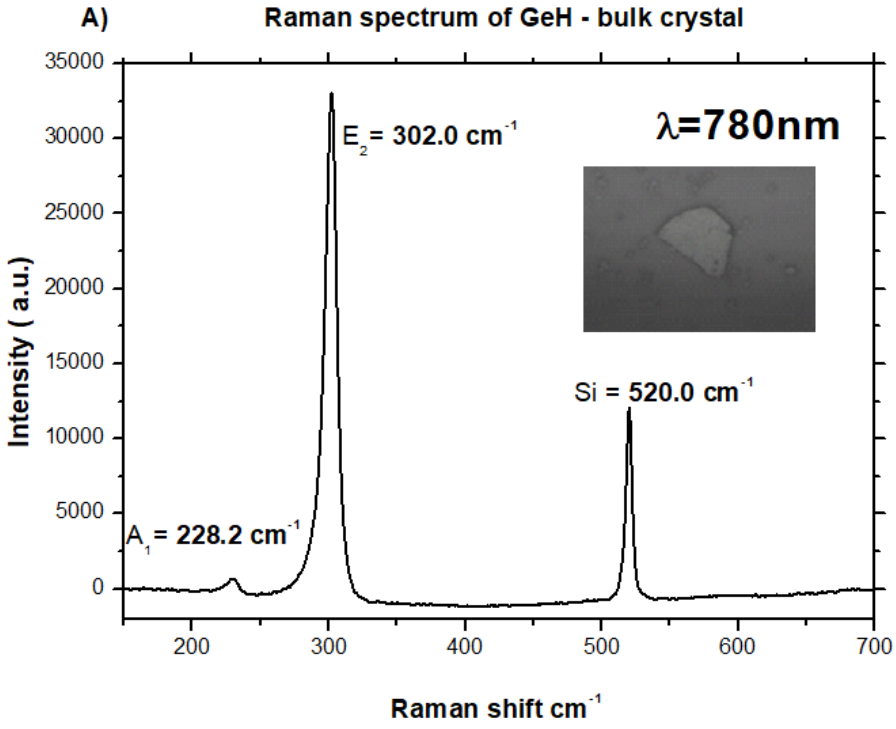
A)
Raman spectrum of GeH - bulk crystal
Intensity (a.u.)
Raman shift cm-1
E2 = 302.0 cm-1
λ=780nm
Si = 520.0 cm-1
A1 = 228.2 cm-1
35000
30000
25000
20000
15000
10000
5000
0
200
300
400
500
600
700

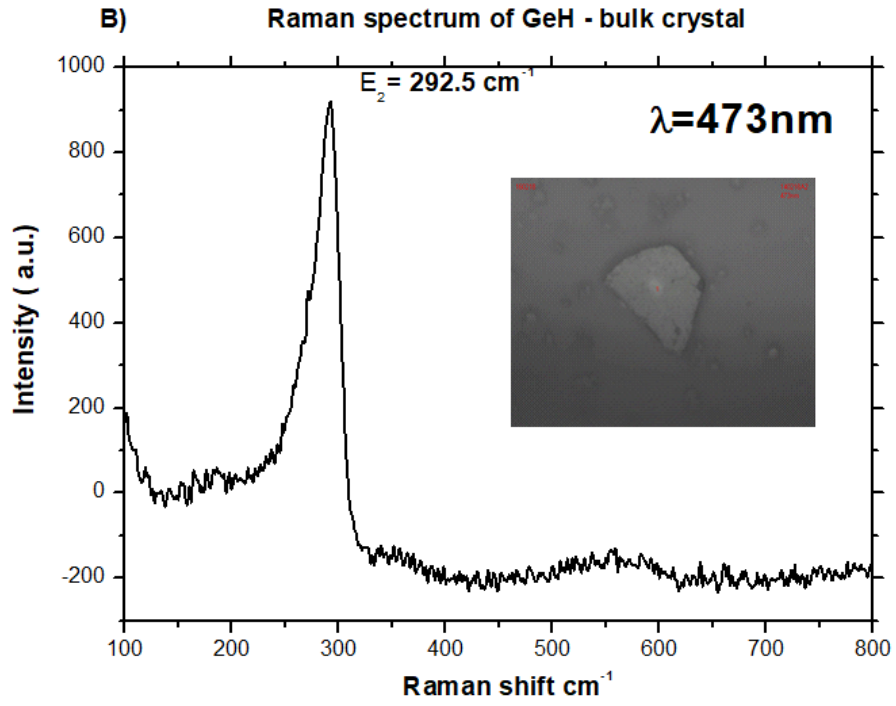
B)
Raman spectrum of GeH - bulk crystal
Intensity (a.u.)
Raman shift cm-1
E2 = 292.5 cm-1
λ=473nm
1000
800
600
400
200
0
-200
100
200
300
400
500
600
700
800

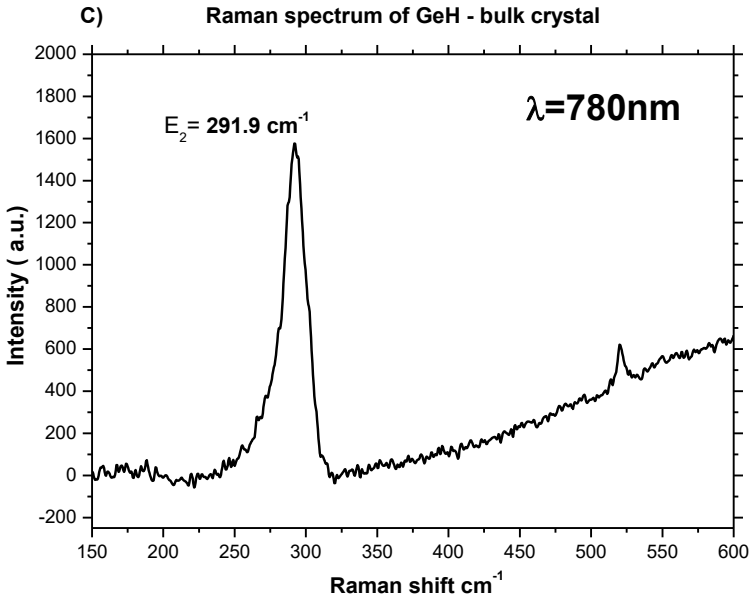

Figure 4.6: A) Raman spectrum of GeH crystal with 780nm excitation. The inset shows an optical image of the sample, B) Raman spectrum of GeH crystal with 473nm wavelength. The A_{1g} peak has disappeared and there is only one peak at 292cm^{-1}. From the optical image of the sample in the inset, it is clear that this laser line has modified the surface of the sample creating a spot. C) Repeat the Raman measurement with the 780nm laser line exactly at the same spot as with the 473nm line. No recovery of the spectrum which indicates that the damage is permanent.

4.1.2 μ – PL spectroscopy

The next step after successfully isolating GeH bulk crystals is to study the temperature dependent optical response via Photoluminescence (PL) and Reflectance Spectroscopy. The sample was cooled down from room temperature (RT) to liquid nitrogen temperature, i.e. 80 K and a PL spectrum was acquired using a 543nm CW excitation energy (Fig.4.7). The PL spectrum is dominated by a single peak at ~1.53 eV assigned to the excitonic transition of the GeH bulk crystal.

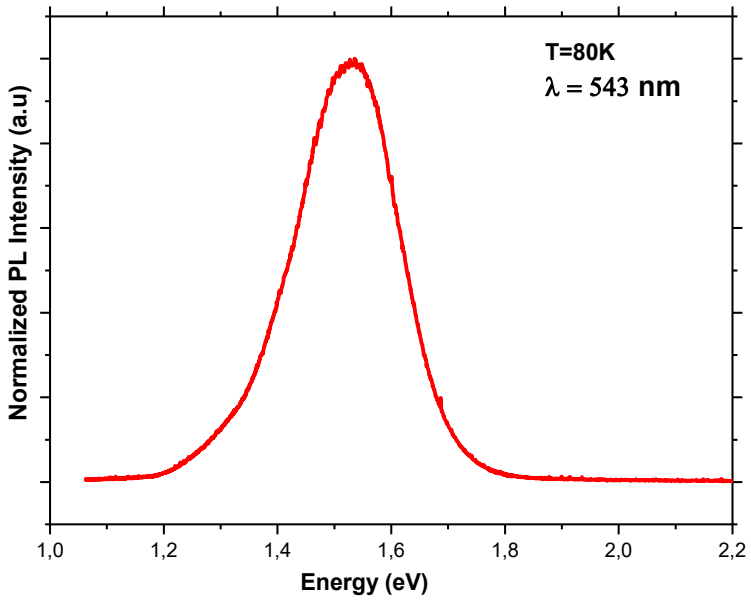

Figure 4.7: a) Photoluminescence spectrum of bulk GeH at 80 K.

Figure 4.8 illustrates the temperature evolution of the normalized PL spectra for the bulk crystal GeH in a temperature range from 80 K to room temperature. With the increase of temperature, the PL peak emission becomes broader in linewidth and red-shifts by almost 110 meV from 80 to 300K. It is noticeable that for higher temperatures, the PL peak consists of two peaks. However, the higher energy peak does not shift with temperature and therefore cannot be associated with the GeH itself and it may come from extrinsic sources other than the sample. In order to better analyze the PL spectra, we deconvolute them into two peaks for temperatures higher than 150K and record the lower energy peak as the PL emission from GeH (Fig.4.9). In addition to the redshift of the PL, there is also a decrease of the total integrated PL intensity by a factor of almost 8 from 80 to 300K.

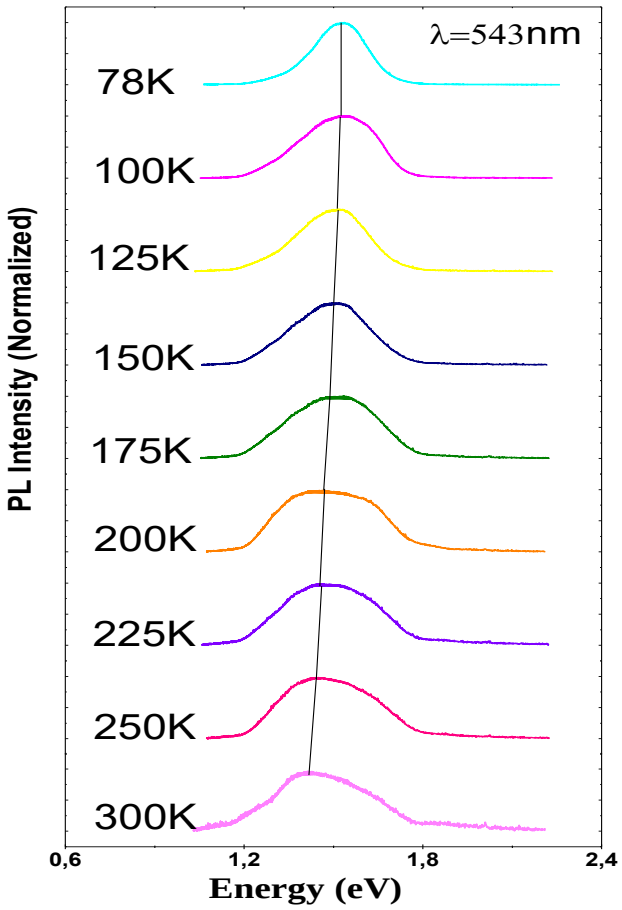

Figure 4.8: Normalized temperature-dependent PL spectra of bulk GeH with 543 excitation wavelength

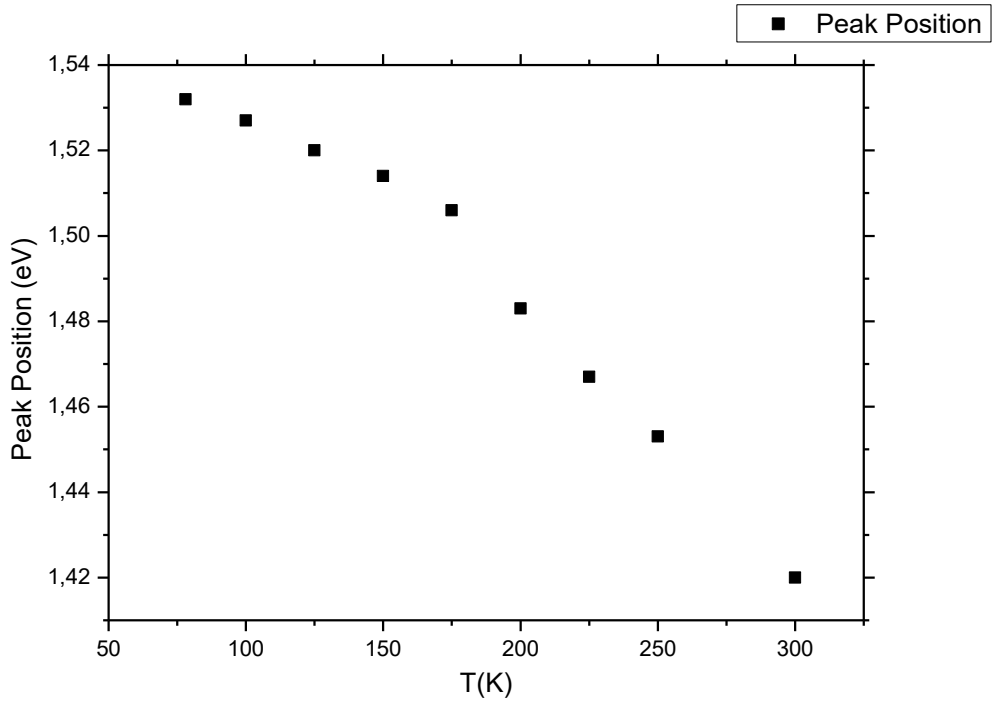

Figure 4.9: Peak Position of temperature-dependent PL spectra of bulk GeH with 543 excitation wavelength

The increase of temperature has a dominant effect on our bulk sample as it results in a progressive red-shift in the exciton emission energies. This behavior is characteristic of semiconductors and can be explained by considering two contributing mechanisms. Firstly, thermal expansion with increasing temperature leads to an increase in the average interatomic distance, therefore shrinking the relative position of the conduction and valence bands. Nevertheless, this effect account for only a small fraction of the observed shifts and sometimes even yields the wrong sign for the thermal expansion coefficient. The major contribution stems from the renormalization of the electronic energies due to a temperature dependent exciton-phonon interaction. As a band to band peak moves within the crystal lattice, it interacts with phonons via scattering processes. There are two principal types of phonon scattering, either phonon absorption or emission. The former is the dominant scattering process at low temperatures when phonons are yet inactive and since only the absorption contributes, the renormalization process becomes temperature independent. However, at temperatures of the order of the Debye temperature or higher, both processes contribute to the exciton scattering causing the exciton energy

to shift as a result of this exciton-phonon interaction [55-57]. This evolution can be described by the Varshni or O'Donnell et al. relations.

Varshni proposed a semi-empirical relation for the variation of the band gap energy, Eg, with temperature, T [55]:

$$E_g(T) = E_{g,o} - \frac{a \cdot T^2}{T + \beta} \qquad \text{Eq. (4.1)}$$

where $E_{g,o}$ is the band gap energy at 0 K and α, β are fitting parameters related to electron-phonon interaction and Debye temperature, respectively. It should be noted that the energy gap is expected to have only slightly changed between absolute zero and the lowest achievable temperature of 80 K in our experiment. Therefore, $E_{g,o}$ is assigned with a value ~10 meV above the band to band resonance at 80 K (i.e. 1.53 eV) and treated as a constant, for the PL analysis. Table 1 shows the best fit values of the parameters α and β for the PL a measurements. The fitted curves obtained are shown in Figure 4.10

Table 1

	Photoluminescence
α (μeV/K)	510
β (K)	337

.

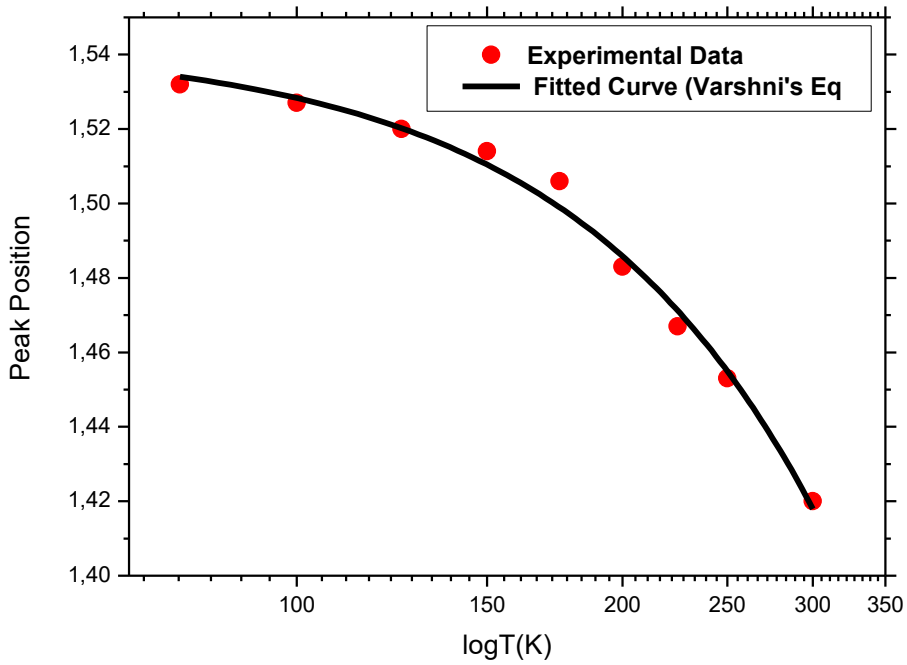

Figure 4.10: Variation of the band to band transition energy with temperature for bulk GeH. Data are extracted from) PL measurements. In each case, red circles represent the transition energy in each temperature while fitted curves using Eq. (4.1) are illustrated as black solid lines.

Alternatively, O' Donnell's equation describes the temperature dependent variation of the gap in terms of a hyperbolic cotangent relation:

$$E_g(T) = E_{g,o} - S\langle\hbar\omega\rangle\left[\coth\left(\frac{\langle\hbar\omega\rangle}{2K_BT}\right) - 1\right] \quad \text{Eq. (4.2)}$$

where S is a dimensionless constant describing the strength of the electron-phonon coupling, K_B is Boltzmann' s constant, and $\langle\hbar\omega\rangle$ is an average phonon energy. The fits to the experimental data are shown in figure 4.9 and the fitting parameters are summarized in Table 2.

Table 2	

	Photoluminescence
S	4,68
$<\hbar\omega>$ (meV)	33.7

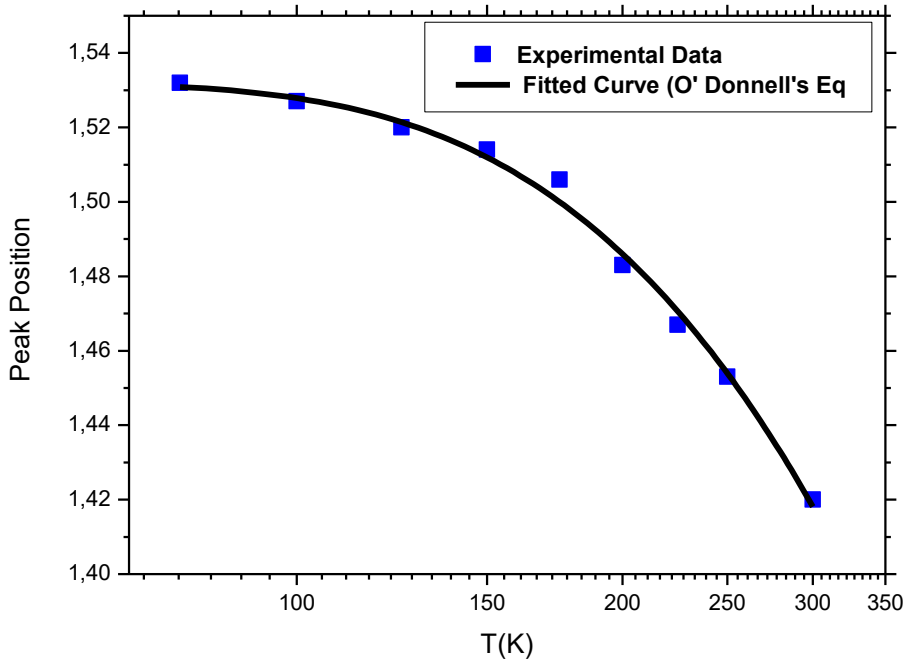

Figure 4.10: Variation of the band to band transition energy with temperature for bulk GeH. Data are extracted from PL measurements. In each case, red circles represent the transition energy in each temperature while fitted curves using Eq. (4.2) are illustrated as black solid lines.

The two previously mentioned models are formulated based on semiconductors with conventional band structure, they can adequately reproduce the band to band transition energies in bulk GeH and other group IV elements, which suggests the independence of the exciton binding energy on temperature.

4.1.3 Reflectivity spectroscopy

In μ – Reflectance spectroscopy the sample is cooled down from room temperature to liquid nitrogen temperature, i.e. 80 K (as in μ – PL measurements). As

we can see below our spectrum (Figure 4.12) shows periodic oscillations due to interference fringes that, unfortunately, completely mask the positon of the excitonic resonance. The y-axis is the ratio of the reflectivity spectra taken on the sample and off the sample from the bare substrate.

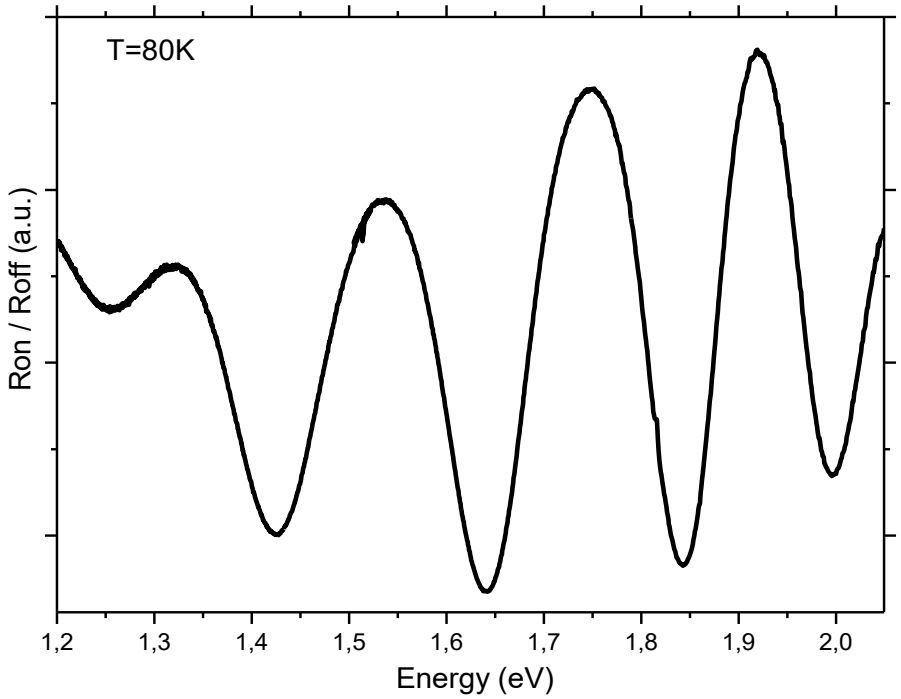

Figure 4.12: μ –Reflectance spectrum of bulk GeH at 80 K.

Interference fringes a bright or dark band caused by beams of light that are in phase or out of phase with one another. Light waves and similar wave propagation, when superimposed, will add their crests if they meet in the same phase (the waves are both increasing or both decreasing); or the troughs will cancel the crests if they are out of phase; these phenomena are called constructive and destructive interference, respectively. If a beam of monochromatic light (all waves having the same wavelength) is passed through two narrow slits, the two resulting light beams can be directed to a flat screen on which, instead of forming two patches of overlapping light, they will form interference fringes, a pattern of evenly spaced alternating bright and dark bands.

A very important information that we can get from the above spectrum is the thickness of the sample we have irradiated. Using the equation

$$(\mathrm{d} = \frac{1}{2 * n * (\frac{1}{\lambda_1} - \frac{1}{\lambda_2})}) \quad \text{Eq.1}$$

where n is Refractive index of our GeH crystal which is 5.02 (from the literature[56]) and λ_1 and λ_2 are the wavelengths of two consecutive maxima or minima in nm. From figure 4.13 where we focus on the range 1.6 to 2 eV, the two consecutive minima are at λ_1 = 1.64eV = 756.09nm and λ_2 = 1.84eV = 672.08 nm, and therefore from the previous equation we get the thickness to be **d = 622.5nm.** This value is very close to values we get for the thickness of the bulk crystals using AFM (550 to 650nm)

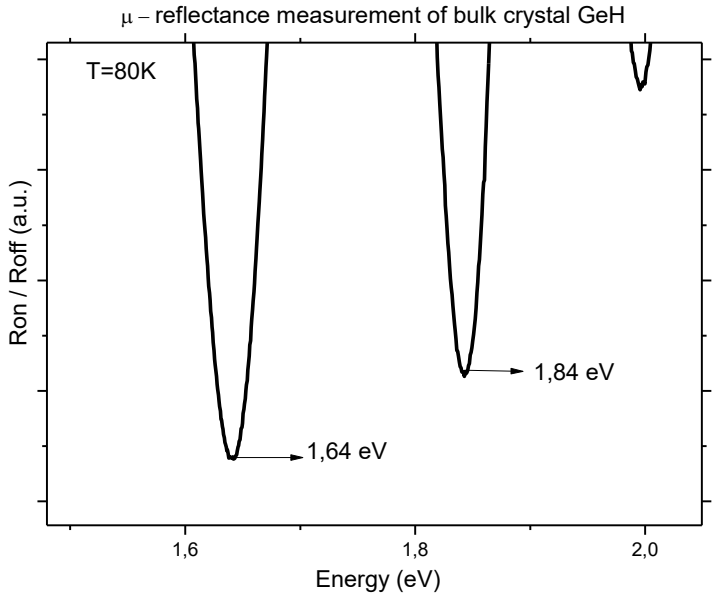

Figure 4.13: μ –Reflectance spectrum of bulk GeH at 80 K.

In a different approach, we can determine the value of the refractive index using the sample thickness we get from AFM. In the next figure (4.14a, b) we see the reflectance spectrum (a) and the AFM measurement (b). From these measurement we will take the thickness d and λ_1, λ_2 so we will calculate the refractive index n.

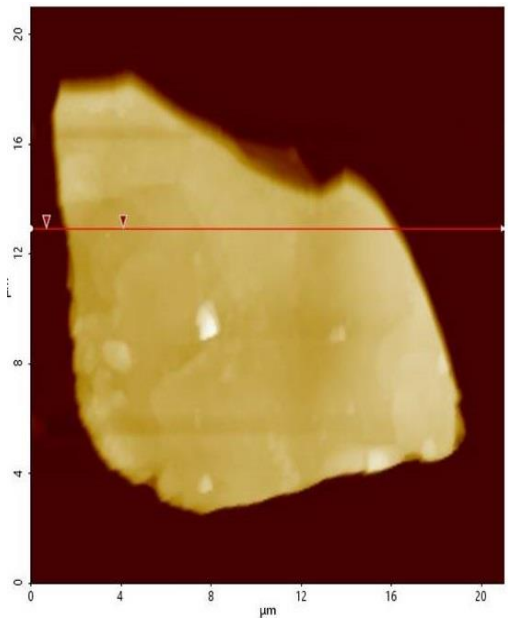
0
4
8
12
16
20
µm

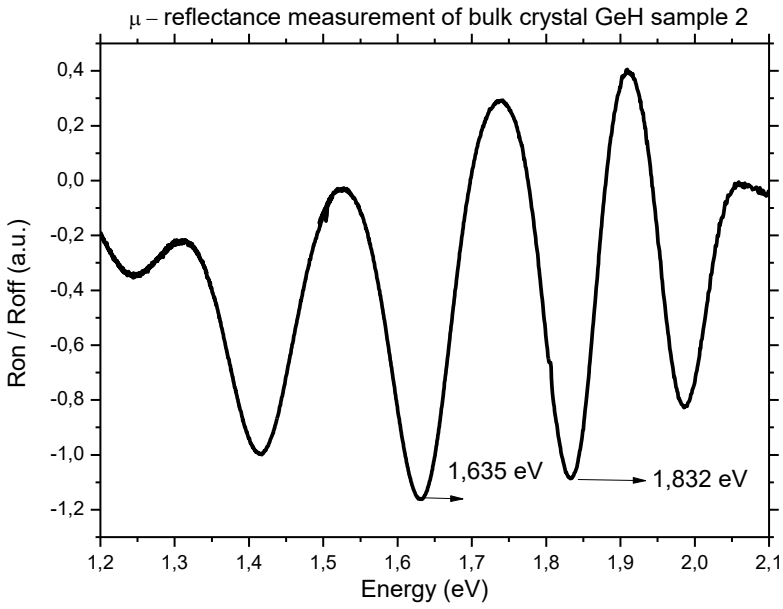
µ – reflectance measurement of bulk crystal GeH sample 2
Ron / Roff (a.u.)
0,4
0,2
0,0
-0,2
-0,4
-0,6
-0,8
-1,0
-1,2
1,635 eV
1,832 eV
1,2
1,3
1,4
1,5
1,6
1,7
1,8
1,9
2,0
2,1
Energy (eV)

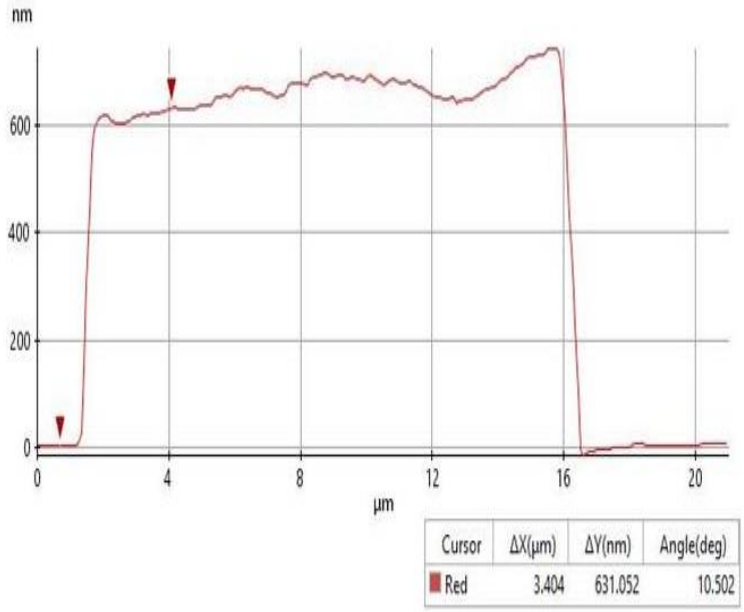

Figure 4.14: μ –Reflectance spectrum of bulk GeH at 80 K (center), AFM image (top) and AFM line scan (bottom). From the line scan we determine a thickness of 631nm.

Using the equation

$$\left(n = \frac{1}{2 * d * \left(\frac{1}{\lambda_1} - \frac{1}{\lambda_2}\right)}\right) \quad \text{Eq.2}$$

where d is the thickness (631nm) and λ_1 and λ_2 are the wavelengths of two consecutive minima in nm. With λ_1 = 1.635eV = **758.40nm** and λ_2 = 1.832eV = **676.85 nm** we get **n = 4.95,** a value very close to 5.02 reported in the literature [56].

Based on our calculations, there is a slight variation in the theoretical value from the literature for the refractive index we have calculated. This is due to an error of possible theoretical calculation performed as well as to the variation in the thickness of the samples. Of course we take into account the experimental value we calculated by knowing the sample thickness by ignoring the theoretical we sought from the literature.

4.2 From bulk to few layers of GeH

After studing the bulk material of GeH, our aim was to study the optical and electronic properties of few layers and even a monolayer of this material. In collaboration with University of Ioannina and the PhD students Nicolaos Chalmpes and Theodosis Giousis (from Professor Gourni's lab) using the technique mentioned in section 3.1 we prepared samples of approximately 2nm thick and performed Raman and Photoluminescence spectroscopy. For the preparation of the samples, we used the ultrasonication method for more than 6 minutes and we increased the amount of solvent and at the same time reduced the amount of powder we used. In Fig.4.15 we see the optical image of the possible single layer of GeH.

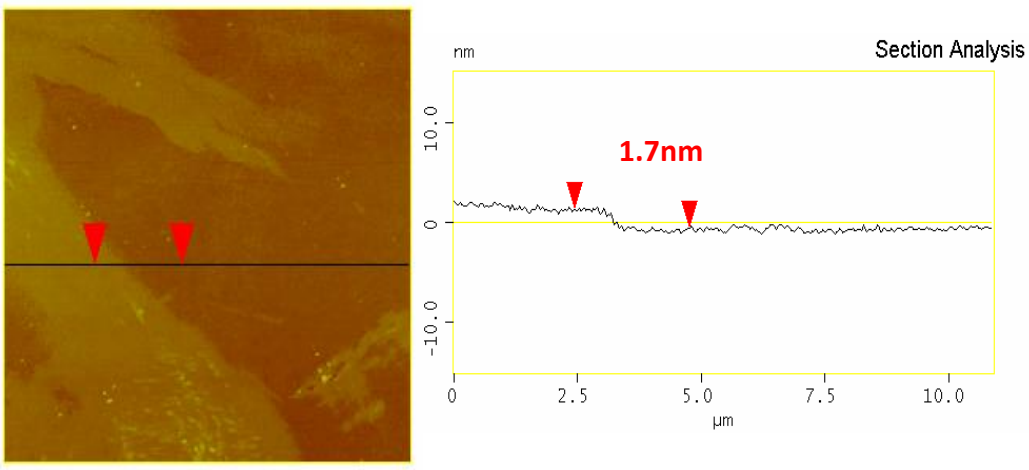

Figure 4.15:Optical microscope image of a monolayer crystal GeH (left), AFM thickness measurement along the black line (right)

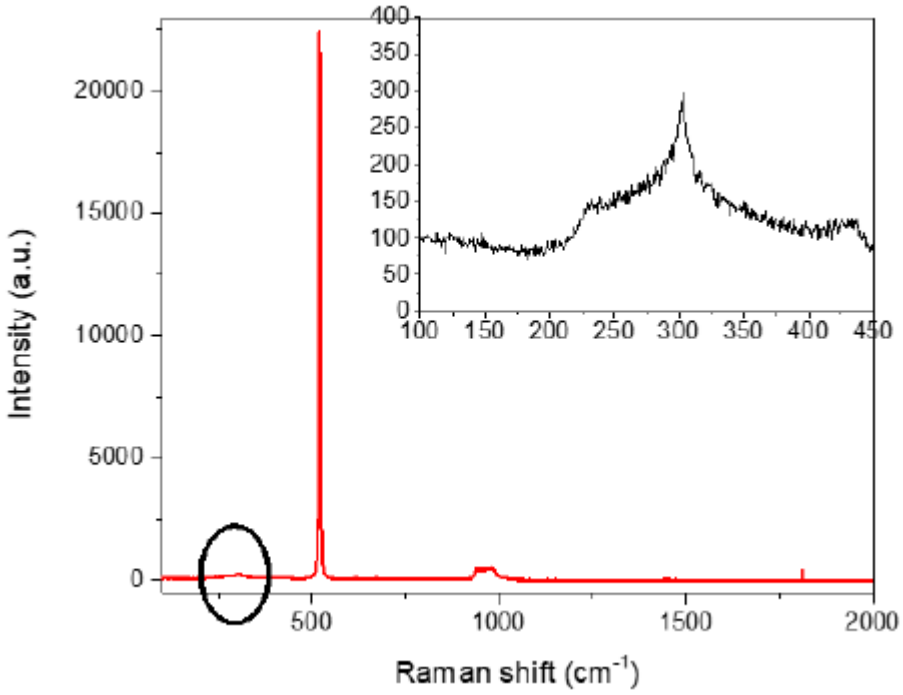

Figure 4.16: Raman spectrum of GeH crystal with 514.5nm wavelength at 300 K.

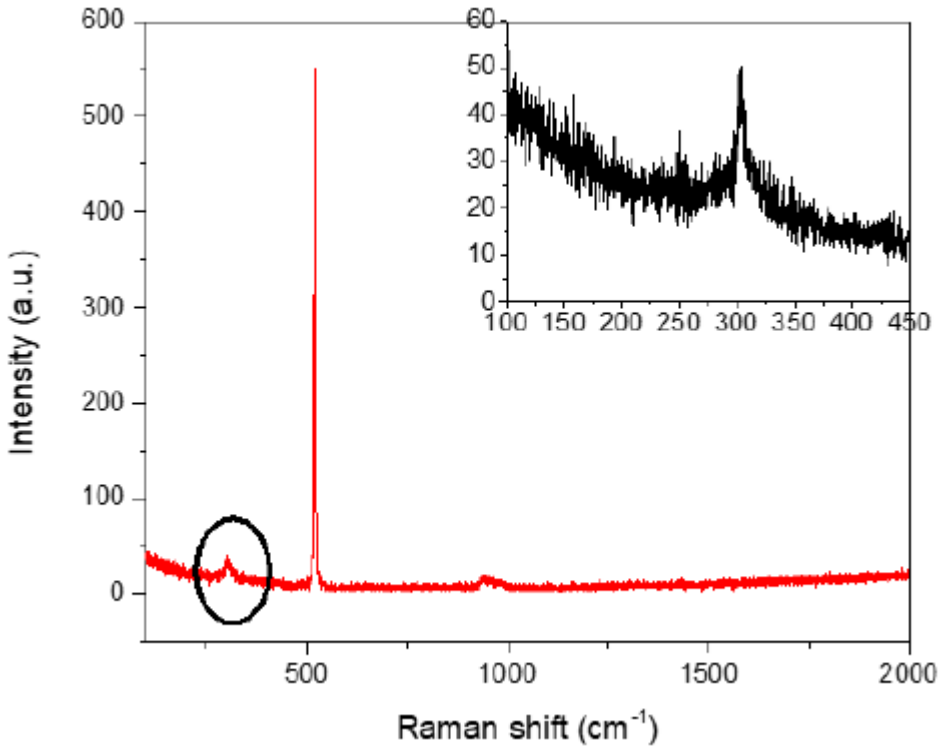

Figure 4.17: Raman spectrum of GeH with 780nm wavelength at 300 K.

Fig. 4.16 shows the Raman spectrum taken with the 514.5nm laser line. The first thing we notice is that the spectrum is dominated by the main Si vibrational mode at 520cm^{-1} and the signal in the energy range of 300cm^{-1} where we expect the modes of GeH is extremely weak. The inset shows in detail this energy range and it is a typical behavior from the Si substrate. The broad band from 230 to 430 cm^{-1} is attributed to the acoustic phonons at specific high symmetry points of the Brillouin zone in Si and the peak at 300 cm-1 is due to 2LA from the X-point. Even in the case there is a signal from the possible single layer, it is extremely weak and masked by the stronger modes of the Si substrate. Changing the laser line from 514.5 to 780 nm didn't change the Raman spectrum (Fig.4.17) and therefore, we conclude that we can't observe the Raman modes of single layer of GeH.

We have also performed PL measurements on the single layer at 80K but there was no emission from the sample.

4.3 Future plan – Future work

The drop-casting technique we used in this thesis results in bulk crystals of the order of 500 to 600 nm. We tried to reduce the thickness of the produced crystals but with no success. From the samples we thought they were single layers, we couldn't get any Raman or PL signal and therefore we couldn't study the optical and electronic properties of monolayer GeH. Therefore, in the future, a different growth approach is needed in order to get thin layers of this material and a special care should be taken to encapsulate the samples before any spectroscopic study.

Part III:
References

[1].Novoselov, K. S.; Geim, A. K.; Morozov, S. V.; Jiang, D.; Zhang, Y.; Dubonos, S. V.*; et al.* Electric Field Effect in Atomically Thin Carbon Films. *Science* **2004,** 306, 666-669.

[2]. Novoselov, K.; Geim, A. K.; Morozov, S.; Jiang, D.; Katsnelson, M.; Grigorieva, I.*; et al.* Two-Dimensional Gas of Massless Dirac Fermions in Graphene. *Nature* **2005,** 438, 197-200.

[3]. Mak, K. F.; Lee, C.; Hone, J.; Shan, J.; Heinz, T. F. Atomically Thin MoS2: a New Direct-Gap Semiconductor. *Phys. Rev. Lett.* **2010,** 105, 136805.

[4]. Splendiani, A.; Sun, L.; Zhang, Y.; Li, T.; Kim, J.; Chim, C.-Y.*; et al.* Emerging Photoluminescence in Monolayer MoS2. *Nano Lett.* **2010,** 10, 1271-1275.

[5]. Butler, S. Z.; Hollen, S. M.; Cao, L.; Cui, Y.; Gupta, J. A.; Gutiérrez, H. R.*; et al.* Progress, Challenges, and Opportunities in Two-dimensional Materials Beyond Graphene. *ACS Nano* **2013,** 7, 2898-2926.

[6]. Elisabeth Bianco, Sheneve Butler, Shishi Jiang, Oscar D. Restrepo, Wolfgang Windl, and Joshua E. Goldberger. Stability and exfoliation of germanane: A germanium graphane analogue. *ACS Nano*, 7(5):4414–4421, 2013. PMID: 23506286.

[7] G., C. Miesner, M.S. Brandt, M. Stutzmann, and G. Abstreiter. Epitaxial alloy films of zintl-phase ca(si1□xgex)2. *Journal of Crystal Growth*, 223(4):573 – 576, 2001.

[8] J.J. Harris, B A. Joyce, and P.J. Dobson. Oscillations in the surface structure of sn-doped gaas during growth by fMBEg. *Surface Science*, 103(1):L90 – L96, 1981.

[9] Shishi Jiang, Sheneve Butler, Elisabeth Bianco, Oscar D Restrepo, Wolfgang Windl, and Joshua E Goldberger. Improving the stability and optical properties of germanane via one-step covalent methyl-termination. *Nature communications*, 5, 2014.

[10] Yandong Ma, Ying Dai, Ying-Bo Lu, and Baibiao Huang. Effective bandgap engineering in wrinkled germanane via tiny electric field. *J. Mater. Chem. C*, 2:1125–1130, 2014.

[11] Branimir Radisavljevic, Aleksandra Radenovic, Jacopo Brivio, V Giacometti, and A Kis. Single-layer MoS_2 transistors. *Nature nanotechnology*, 6(3):147–150, 2011.

[12] Oscar D Restrepo, Kevin E Krymowski, Joshua Goldberger, and Wolfgang Windl. A first principles method to simulate electron mobilities in 2d materials. *New Journal of Physics*, 16(10):105009, 2014.

[13] Chen Si, Junwei Liu, Yong Xu, Jian Wu, Bing-Lin Gu, and Wenhui Duan. Functionalized germanene as a prototype of large-gap two-dimensional topologicalinsulators. *Phys. Rev. B*, 89:115429, Mar 2014.

[14]. Rivillon, S.; Chabal, Y. J.; Amy, F.; Kahn, A. Hydrogen Passivation of Germanium (100) Surface Using Wet Chemical Preparation. *Appl. Phys. Lett.* **2005,** 87, 253101.

[15]. Kresse, G.; Hafner, J. Ab Initio Molecular Dynamics for Liquid Metals. *Phys. Rev. B* **1993,** 47, 558-561.

[16]. Kresse, G.; Hafner, J. Ab Initio Molecular-Dynamics Simulation of the Liquid-Metal-Amorphous-Semiconductor Transition in Germanium. *Phys. Rev. B* **1994,** 49, 14251-14269.

[17]. Mak, K. F.; Lee, C.; Hone, J.; Shan, J.; Heinz, T. F. Atomically Thin MoS2: A New Direct-Gap Semiconductor. *Phys. Rev. Lett.* **2010,** 105, 136805.

[18]. Lee, P. A.; Said, G.; Davis, R.; Lim, T. On the Optical Properties of Some Layer Compounds. *J. Phys. Chem. Solids* **1969,** 30, 2719-2729.

[19]. Gaiser, C.; Zandt, T.; Krapf, A.; Serverin, R.; Janowitz, C.; Manzke, R. Band-Gap Engineering with HfSxSe2− x. *Phys. Rev. B* **2004,** 69, 075205.

[20]. Vogg, G.; Meyer, A. J. P.; Miesner, C.; Brandt, M. S.; Stutzmann, M. Efficient Tunable Luminescence of SiGe Alloy Sheet Polymers. *Appl. Phys. Lett.* **2001,** 78, 3956-3958.

[21]. Blöchl, P. E. Projector Augmented-Wave Method. *Phys. Rev. B* **1994,** 50, 17953-17979.

[22]. Perdew, J. P.; Burke, K.; Ernzerhof, M. Generalized Gradient Approximation Made Simple. *Phys. Rev. Lett.* **1996,** 77, 3865-3868.

[23]. Perdew, J. P.; Burke, K.; Ernzerhof, M. Generalized Gradient Approximation Made Simple [Phys. Rev. Lett. 77, 3865 (1996)]. *Phys. Rev. Lett.* **1997,** 78, 1396-1396.

[24]. Grimme, S. Semiempirical GGA-Type Density Functional Constructed with a Long-Range Dispersion Correction. *J. Compt. Chem.* **2006,** 27, 1787-1799.

[25]. Heyd, J.; Scuseria, G. E.; Ernzerhof, M. Hybrid Functionals Based on a Screened Coulomb Potential. *J. Chem. Phys.* **2003,** 118, 8207-8215.

[26]. Heyd, J.; Scuseria, G. E.; Ernzerhof, M. Hybrid Functionals Based on a Screened Coulomb Potential. [Erratum to Document Cited in CA139:042043]. *J. Chem. Phys.* **2006,** 124, 219906.

[27]. Paier, J.; Marsman, M.; Hummer, K.; Kresse, G.; Gerber, I. C.; Angyan, J. G. Screened Hybrid Density Functionals Applied to Solids. *J. Chem. Phys.* **2006,** 124, 154709.

[28]. Deegan, T.; Hughes, G. An X-ray Photoelectron Spectroscopy Study of the HF Etching of Native Oxides on Ge (111) and Ge (100) Surfaces. *Appl. Surf. Sci.* **1998,** 123, 66-70.

[29]. Bodlaki, D.; Yamamoto, H.; Waldeck, D.; Borguet, E. Ambient Stability of Chemically Passivated Germanium Interfaces. *Surf. Sci.* **2003,** 543, 63-74.

[30]. Nicholas D. Cultrara, Yaxian Wang, Maxx Q. Arguilla, Michael R. Scudder, Shishi Jiang, Wolfgang Windl, Svilen Bobev, Synthesis of 1T, 2H, and 6R Germanane Polytypes Chem. Mater. 2018, 30, 1335−1343

[31] C.V. Raman and K.S. Krishnan, Nature, A New Type of Secondary Radiation, 121, 501 (1928)

[32] J. R. Ferraro, K. Nakamoto and C. W. Brown, Introductory Raman Spectroscopy, Elsevier, 2003 (Second Edition)

[33] E. Smith and G. Dent, Modern Raman Spectroscopy - A Practical Approach, John Wiley & Sons, Ltd, 2005

[34] Houssa M, Scalise E, Sankaran K, Pourtois G, Afanasev V V and Stesmans A 2011 Appl. Phys. Lett. 98 223107

[35] Garcia J C, de Lima D B, Assali L V C and Justo J F 2011 J. Phys. Chem. C 115 13242

[36] Pulci O, Gori P, Marsili M, Garbuio V, Del Sole R and Bechstedt F 2012 Europhys. Lett. 98 37004

[37] Wei W and Jacob T 2013 Phys. Rev. B 88 045203

[38] Sofo J O, Chaudhari A S and Barber G D 2007 Phys. Rev. B 75 153401

[39] Park S, Lee B, Jeon S H and Han S 2011 Curr. Appl. Phys. 11 S337

[40] B.G. Streetman and S. K. Banerjee, Solid State Electronic Devices, Pearson, 7th Edition (Global Edition)

[41] Mark Fox, Optical Properties of Solids, Oxford University Press, 2nd edition (2010)

[42] M. Grundmann, The Physics of Semiconductors: An Introduction Including Devices and Nanophysics, Springer 2nd edition (2010)

[43] Original image taken from presentation: D. Lidzay, Optical Spectroscopy, Retrieved from: https://www.slideshare.net/cdtpv/optical-spectroscopy-56823999

[44] K. F. Mak, M. Y. Sfeir, Y. Wu, C. H. Lui, J. A. Misewich, and T. F. Heinz, Measurement of the Optical Conductivity of Graphene, Phys. Rev. Lett. 101, 196405 (2008)

[45] R. Frisenda, Y. Niu, P. Gant, A. J. Molina-Mendoza, R. Schmidt, R. Bratschitsch, J. Liu, L. Fu, D. Dumcenco, A. Kis, D. Perez De Lara and A. Castellanos-Gomez, Micro-reflectance and transmittance spectroscopy: a versatile and powerful tool to characterize 2D materials, J. Phys. D: Appl. Phys. 50 074002 (2017)

[46] P. Yu, M. Cardona, Fundamentals of Semiconductors: Physics and Materials Properties, Springer, 2010 (Fourth edition)

[47] Horiba Scientific, Photoluminescence (PL), Retrieved from: http://www.horiba.com/scientific/products/photoluminescence/ (Accessed: 25/12/2017)

[48] Horiba Group, High-Resolution Low-Temperature PL of Semiconductors, Available at: Resolution_Low-Temperature_PL_of_Semiconductors_2013.PDF (Accessed: 25/12/2017)

[49] M.M. Benameur, B. Radisavljevic, J.S. Heron, S. Sahoo, H. Berger, A. Kis, Visibility of dichalcogenide nanolayers, Nanotechnology 22, 125706 (5pp) (2011)

[50] Park XE7: User's Manual, Version 2.2 (2016)

[51] Tapping Mode AFM, Retrieved from (27/01/2018):http://www.nanophys.kth.se/

[52] What is a confocal Raman microscope? Exctracted from what-is-a-confocal-raman-microscope/

[53] Nicolet Almega XR: High-Performance Dispersive Raman Spectrometers, Nicolet-Almega-XR-dispersive-Raman-microscope-brochure.pdf

[54] C.Serino, S.Ko, T.Yeung et all: Lithium-Ion Insertion Properties of Solution-Exfoliated Germanane ACS Nano 2017, 11, 7995−8001

[55] Y.P. Varshni, Temperature dependence of the energy gap in semiconductors, Physica 34, Issue1, p. 149-154 (1967)

[56] W. Zhao, R. M. Ribeiro, M. Toh, A. Carvalho, C. Kloc, A. H. Castro Neto and G. Eda, Origin of Indirect Optical Transitions in Few-Layer MoS2, WS2, and WSe2, Nano Lett., 13 (11), pp 5627‐5634 (2013)

[57] K. P. O' Donnell and X. Chen, Temperature dependence of semiconductor band gaps, Appl. Phys. Lett. 58, 2924 (1991)